Food Research International 206 (2025) 116047

Contents lists available at ScienceDirect

Food Research International

journal homepage: www.elsevier.com/locate/foodres

Integrated use of ultrasound imaging and multivariate image analysis for detecting bone fragments in poultry meat

Gentil A. Collazos-Escobar [a], Elisa Lincetti [b], Sara Spilimbergo [b], José M. Prats-Montalbán [c], José V. García-Pérez [a], José Benedito [a,*]

[a] Grupo de Análisis y Simulación de Procesos Agroalimentarios (ASPA), Instituto Universitario de Ingeniería de Alimentos–FoodUPV, Universitat Politècnica de València, Camí de Vera s/n, Edificio 3F, 46022, Valencia, Spain.
[b] Department of Industrial Engineering, University of Padova, Padova, 35131, Italy
[c] Grupo de Ingeniería Estadística Multivariante (GIEM), Universitat Politècnica de València (UPV), Camino de Vera s/n, Edificio 7A, 46022, Valencia, Spain

ARTICLE INFO

Keywords:
Foreign bodies
Chicken
In-line quality monitoring
Ultrasound imaging
Multivariate image analysis
Multivariate statistical process control

ABSTRACT

Poultry meat industry requires intelligent systems for achieving non-invasive real-time detection of bone fragments. Therefore, the main aim of this study was to assess the feasibility of using ultrasound imaging and multivariate image analysis to detect bone fragments in boneless and skinless chicken breast fillets. Bone fragments of different sizes were inserted into the chicken and contact ultrasound images were acquired, following a pre-established pattern, in the control (C) and out-control (OC, with bone) samples, by scanning the breast's surface, using contact ultrasound sensors (1 MHz) working in through transmission. Energy-magnitude and energy-distribution ultrasound parameters were computed at pixel level in time (TDA) and frequency domain (FDA). Principal Component Analysis (PCA) was used in TDA and FDA parameters, and its combination (TFDA). From PCA model, the Residual Sum Squares (RSS) and Hotelling's T-square (T^2) control statistics were used to classify the C and OC images projected on the PCA latent structure. Experimental results demonstrated that the presence of bone fragments within chicken breast fillets led to alterations in the energy-magnitude (avg. amplitude decrease from 81.6 % to 52.6 %, depending on the bone size) and energy-distribution ultrasound parameters (avg. variance decreased from 97.9 % to 70.6 % depending on the bone size). The RSS statistic achieved the best classification performance (accuracy of TDA, FDA and TFDA>95 %) in C and OC images. These results highlight the potential of combining contact ultrasound imaging with multivariate image analysis for the reliable and rapid detection of bone fragments in chicken breasts.

1. Introduction

The poultry meat industry has undergone a rapid expansion in recent years, and it is currently the most produced meat worldwide (Aggrey et al., 2023; Fang et al., 2023). The consumption of poultry meat is increasing, due to its affordability and high nutritional value (Jiang et al., 2018). However, poultry meat production encounters several challenges, related to the assurance of product quality and safety. Moreover, another relevant concern is avoiding the presence of foreign bodies in the final manufactured products. Foreign bodies represent a physical risk in food safety, and in the poultry meat industry (Nielsen et al., 2013), bone fragments (BF) are a persistent problem. Different techniques, such magnetic detectors, X-rays, and hyperspectral sensors, have been extensively used in the detection of foreign bodies within food products (Yaqoob et al., 2021). These methods come with certain limitations for food inspection, such as the high cost of equipment and maintenance, challenges associated with their integration into food processing lines, and, in some cases, limited penetration capability to thoroughly analyze the internal structure of food (Pérez-Santaescolástica et al., 2019).

Ultrasound has been employed as a valuable tool for the non-destructive testing of food materials. Ultrasound offers advantages over the aforementioned technologies: it enables faster inspection, it is cost-efficient, versatile, easy to manipulate, safe for personnel, and suitable for real-time in-line application (Fariñas, Contreras, et al., 2021). Consequently, the US has emerged as a promising technology for detecting foreign bodies in foods. The conventional method for analyzing food products and processes rely on the contact ultrasonics

* Corresponding author.
E-mail address: jjbenedi@tal.upv.es (J. Benedito).

https://doi.org/10.1016/j.foodres.2025.116047
Received 11 December 2024; Received in revised form 17 February 2025; Accepted 21 February 2025
Available online 23 February 2025

technology. In contact ultrasonics, sensors require close contact with the food material to eliminate air gaps at the sensor-sample interface and enhance energy transfer into the sample. This contact is achieved through the use of coupling materials such as water, oil, or glycerine (Sanchez-Jimenez et al., 2023) and/or by applying a slight static pressure. In the meat sector, contact ultrasonics measurements have been satisfactorily employed for monitoring the physicochemical modifications in beef steaks during the dry salting process (Fariñas et al., 2023), for on-line monitoring of the ham salting process (Garcia-Perez et al., 2019) or for the characterization of dry-cured ham (Corona et al., 2013), among other applications (Gao et al., 2024; Grassi et al., 2024; Sun et al., 2023). Regarding the detection of BF in chicken breast, Correia et al. (2008) designed and assembled an ultrasonic system based on contact ultrasonics in pulse-echo mode. The effectiveness of their system showed an acceptable detection of fragments ranging from 6 mm^2 to 16 mm^2. However, important limitations related with experimental variability, leading to inconsistent and unreliable measurements.

An additional benefit of ultrasound lies in its capacity for spatial analysis of food products by creating ultrasound images (USI). USI serves as a valuable non-destructive tool for inspecting food by scanning the surface of the product (Gan, 2020). It offers a spatial representation of internal characteristics, facilitating the evaluation of physicochemical attributes related to composition, texture or internal irregularities, such as the foreign bodies presence. The massive volume of data generated by using USI requires robust computing models to extract relevant information. In this sense, pattern recognition techniques constitute an advanced tool (Ozturk et al., 2023), and are classified into two categories: unsupervised techniques and supervised techniques (Jiménez-Carvelo et al., 2019). The principal component analysis (PCA) is one of the most unsupervised techniques used not only for exploratory analysis purposes, but also is the basis for applying the multivariate image analysis (MIA) procedure. MIA is mostly considered a valuable statistical methodology for understanding the relationships and structures within datasets (Duchesne et al., 2012). Furthermore, MIA-based Statistical Process Control (SPC) can be applied for process monitoring and foreign bodies detection based on an image (Prats-Montalbán et al., 2011). The integration of US and Pattern recognition supervised techniques has been previously employed in various applications, including the monitoring of yogurt fermentation process (Bowler et al., 2023), tracking the drying of potato slices (Sanchez-Jimenez et al., 2023), the detection of internal cracks in Manchego cheese (Conde et al., 2008), and has also been used for assessing the coconut maturity (Caladcad et al., 2020). However, the calibration of these models required the use of a latent space (latent variables- LVs, from PCA) as an input of those techniques (Jiménez-Carvelo et al., 2019), which means an additional calculation in the setting of the optimal number of the LVs and the optimization of the hyperparameters belonging to each supervised technique, to achieve the model's goal. Therefore, using PCA as an analytical tool can circumvent the abovementioned issues. There is a notable gap in the existing literature regarding the integration of MIA-based SPC and USI for aiding in the detection of foreign bodies in food products. In particular, the integration of MIA and USI for the detection of BFs in poultry meat has not been previously addressed. Therefore, this work aims to investigate the feasibility of utilizing contact USI and MIA parameters for the detection of varying-sized BF in chicken breast.

2. Materials and methods

2.1. Chicken breast samples

Skinless and boneless chicken breast samples were purchased from a local grocery store in Valencia (Spain) and kept in refrigeration at 4 °C until use (Fig. 1A). The fresh breasts were then cut into 5 × 5 cm fillet samples with a thickness of about 1.5 cm (Fig. 1B). Fresh fillet samples with no BF were considered as the control samples.

2.2. Bone fragments

A BF set extracted from different parts of the chicken skeleton was used. For this purpose, a whole chicken was purchased, boiled for 20 min at 80 °C, and then manually deboned, in order to only extract BF. The remaining boiled chicken was discarded, as the analyses were conducted exclusively on fresh chicken samples, as described in section 2.1.

The BF used in the experiments (Fig. 1E) consisted of a bone obtained from dorsal vertebrae with dimensions of 2.0 × 1.5 cm (Fig. 1Ei), a fragment taken from the chest bone of 2.0 × 1.0 cm (Fig. 1Eii), and three different fragments extracted from the chicken rib with sizes of 1.5 × 0.3 cm (Fig. 1Eiii), 1.0 × 0.3 cm (Fig. 1Eiv) and 0.5 × 0.3 cm (Fig. 1Ev). Dimensions make reference to maximum height and width of BF.

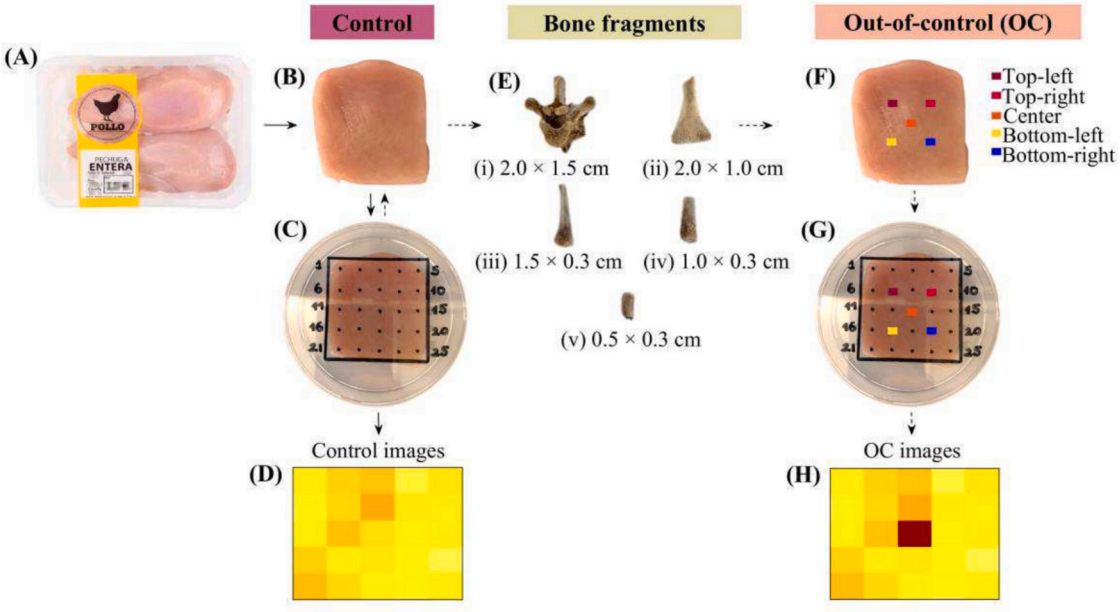

Fig. 1. Flowchart of the main steps to prepare control and OC (out-of-control) samples. A, B, C and D for control images, and C, B, E, F, G and H for OC images.

2.3. Ultrasound experimental set-up

USI were acquired using the experimental set-up illustrated in Fig. 2. The equipment consisted of a computer (Fig. 2A), an oscilloscope (Fig. 2B, MDO3024, Tektronix, WA, USA), an ultrasonic pulser-receiver (Fig. 2C, 5077 PR, Olympus, Houston, TX, USA), a pair of commercial ultrasound transducers (Fig. 2D, A314S-SU model, Panametrics, Waltham, MA, USA) of 1 MHz central frequency and 1 cm of diameter, operating in through-transmission mode and a digital caliper (Fig. 2F, 192–633 Serie, Mitutoyo, Japan). A program was developed in LabVIEW® 2018 (National Instruments, Austin, TX, USA) to record the ultrasonic signals from the oscilloscope.

2.4. Experimental procedure

Control samples fillets (without BF) were placed in polystyrene plates (86.4 ± 0.1 mm diameter, 14 ± 0.1 mm thickness) (Fig. 1C) in order to measure the ultrasound signals in the same locations for each sample, thus obtaining the USI. To achieve this, on the surface of polystyrene plates, a pre-established pattern was previously drawn consisting on a matrix of 25 points (5 × 5 cm) separated every 1 cm (Fig. 1C). Each point of this matrix corresponded to a pixel of the image (Fig. 1D). After ultrasonic measurements were performed, each type of BF was inserted into the previously measured control samples, using a laboratory forceps, trying to place it equidistant from each face of the chicken breast sample. Each BF was placed in five different locations (Fig. 1F), namely, the top-left, top-right, center, bottom-left and bottom-right, corresponding to the position 7, 9, 13, 17 and 19 of the pre-established matrices (Fig. 1G), respectively. Thus, OC ultrasound images (Fig. 1H) were obtained. USI was obtained for the different BF (n = 5, Fig. 1E) in triplicate (n = 3) placed in each location (n = 5, Fig. 1F). Thus, a total of 75 chicken samples (5 × 5 × 3) were needed. Six additional samples were measured to increase the number of observations; thus, 81 chicken breast samples (Fig. 1B) were analyzed.

In each measurement point (Fig. 1C), two types of ultrasound signals (10 k points, average of 128 acquisitions) in the time-domain were obtained. The first one was acquired with gain of −20 dB and used to compute the energy-related ultrasound parameters in the time (section 2.5.1) and frequency (section 2.5.2) domains. Then, a second type of ultrasound signal was acquired with a gain of 0 dB (Fig. 2C) to calculate the ultrasound velocity (section 2.5.1). Thus, two types of 3D images of 5 × 5 cm (spatial dimensions-2D of scanned product's surface) × 10 k points (measured ultrasound signal at each point-1D) were acquired in every run. Moreover, the thickness of the samples was gathered for each pixel using the digital caliper.

2.5. Feature extraction

Different parameters related to energy and also the ultrasonic velocity was computed at pixel level, thus, each parameter summarized a channel of the image. As an example, if six parameters were estimated from a 3D image, a new image of 5 × 5 (spatial dimensions) × 6 (computed parameters) may be obtained.

2.5.1. Time domain analysis

Energy-magnitude ultrasound parameters such as peak-to-peak distance (PP, V), energy (ENG, V^2) and integral of signals (INT, V μs) (Bowler et al., 2023) and ultrasound velocity (V_e, m/s) were computed in the time-domain. The INT was computed by using the trapezoidal numerical method "trapz" of MATLAB® R2023a (The MathWorks Inc., Natick, MA, USA). The Variance (VAR_t, V^2), skewness (SKE_t), kurtosis (KUR_t) and entropy (ENT_t) of ultrasound signals were also computed using "var", "skewness", "kurtosis" and "entropy" MATLAB functions (Caesarendra & Tjahjowidodo, 2017).

$$PP = max(X_t) - max|min(X_t)| \quad (1)$$

$$ENG = \|X_t\|^2 \quad (2)$$

$$INT = \sum_{i=1}^{N} Xz_{t_i} t_i \quad (3)$$

$$VAR_t = \frac{\sum_{i=1}^{N} (X_{t_i} - \overline{X_t})^2}{(N-1)} \quad (4)$$

$$SKE_t = \frac{\left[\sum_{i=1}^{N} (X_{t_i} - \overline{X_t})^3\right] / (N-1)}{\sigma_t{}^3} \quad (5)$$

$$KUR_t = \frac{\left[\sum_{i=1}^{N} (X_{t_i} - \overline{X_t})^4\right] / (N-1)}{\sigma_t{}^4} \quad (6)$$

$$ENT_t = -\sum_{i=1}^{N} p(X_{t_i}) log_2 p(X_{t_i}) \quad (7)$$

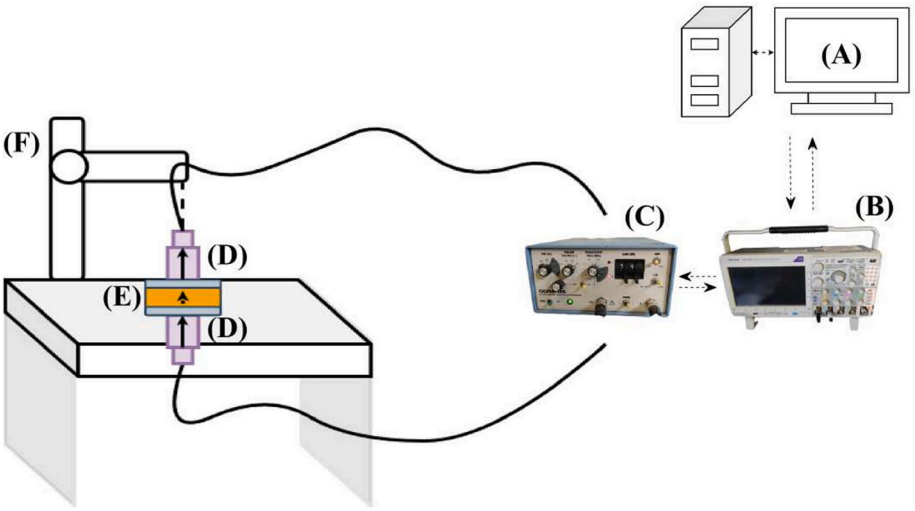

Fig. 2. Ultrasound image acquisition device: Computer (A), oscilloscope (B), generator-receiver (C), ultrasonic transducers (D), food sample (E) and digital caliper (F).

Where X_t is the ultrasound signal in the time-domain, Xz_t corresponded with the positive values of X_t, $\bar{X}_t$ is the mean of each ultrasound signal in the time-domain, N is the number of elements of each X_t, t is the vector which registered the ultrasound signal's traveling time (μs), σ_t the standard deviation of each ultrasound signal in time-domain and $p(X_{ti})$ is the probability of the occurrence of the *i*-th amplitude value in the discretized time-domain ultrasound signal. To assess the V_e (Eq. 8), the time of flight (TOF, μs) was firstly calculated by using Eq. 9 following the energy threshold method (ETM) described by Garcia-Perez et al. (2019).

$$Vel = \frac{L}{TOF} \tag{8}$$

$$TOF = \frac{(TOA - T_r)}{ae} \tag{9}$$

Where L (m) is the thickness in the measurement point; TOA, the arrival time (points) of the ultrasonic signal; T_r, the trigger location (points) and ae (100 Mpoints/s) the acquisition speed.

2.5.2. Frequency domain analysis

The Fast Fourier Transform (FFT) was applied on the time-domain ultrasound signals to obtain the ultrasound frequency spectrum (phs, computed via "fft", MATLAB function, Eq. 10). From phs, the following energy related ultrasound parameters in the frequency domain were computed. Zero-order moment (M_0, MHz, Eq. 11) corresponded with the integral of the area under the curve of the phs (Garcia-Perez et al., 2019). The first-order moment (M_1, MHz) was calculated using Eq. 12, while the ratio M_0/M_1 computes the center frequency (F_r) of the phs (Eq. 13). Additionally, the maximum peak of the frequency spectrum (MP, Eq. 14) was also considered. As in section 2.5.1, the spectral-variance (VAR_{sp}, Eq. 15), spectral-skewness (SKE_{sp}, Eq. 16), spectral-kurtosis (KUR_{sp}, Eq. 17) and spectral-entropy (ENT_{sp}, Eq. 18) were also determined (Caesarendra & Tjahjowidodo, 2017).

$$phs = |FFT| \tag{10}$$

$$M_0 = \sum_{f=1}^{N=f_{FFT}} phs(f)\,\Delta f \tag{11}$$

$$M_1 = \sum_{f=1}^{N=f_{FFT}} phs(f)\,f^r \Delta f \tag{12}$$

$$F_r = \frac{M_1}{M_0} \tag{13}$$

$$MP = max(phs) \tag{14}$$

$$VAR_{sp} = \frac{\sum_{i=1}^{N} (phs_i - \overline{phs})^2}{(N-1)} \tag{15}$$

$$SKE_{sp} = \frac{\left[\sum_{i=1}^{N} (phs_i - \overline{phs})^3\right] \Big/ (N-1)}{{\sigma_{sp}}^3} \tag{16}$$

$$KUR_{sp} = \frac{\left[\sum_{i=1}^{N} (phs_i - \overline{phs})^4\right] \Big/ (N-1)}{{\sigma_{sp}}^4} \tag{17}$$

$$ENT_{sp} = -\sum_{i=1}^{N} p(phs_i) log_2 p(phs_i) \tag{18}$$

Where f is the vector of spectral frequencies (MHz), f_{FFT} is the maximal frequency obtained by using the FFT, r represents the order of the moment, $\overline{phs}$ is the mean of each phs, σ_{sp} the standard deviation of each phs and $p(phs_i)$ is the probability of the occurrence of the *i*-th value in the discretized phs.

2.5.3. Statistical analysis

In order to assess the influence of BF size/type and their location within chicken breast fillets on the time and the frequency domain ultrasound parameters, a multifactor analysis of variance (ANOVA) was considered. The mean pairwise comparisons were performed by using Fisher's Least Significant Difference (LSD) test with a 95 % confidence interval. Further, an ANOVA test based on L values was also performed to examine whether the inserted BFs affected the thickness of measured samples.

2.6. Multivariate image analysis

In order to assess the feasibility of using the USI to detect BF, three different approaches were proposed i) time-domain (TDA), frequency-domain (FDA) and combined time-frequency domain (TFDA). TDA approach used all the parameters computed in the time-domain (PP, ENG, INT, V_e, VAR_t, SKE_t, KUR_t and ENT_t), while FDA used the ones in the frequency-domain (M_0, F_r, MP, VAR_{sp}, SKE_{sp}, KUR_{sp} and ENT_{sp}). Additionally, in order to determine the influence of the number of images used to detect the BF, four different datasets were used considering 100 %, 75 %, 50 % and 25 % of the experimental data (81 control and 81 OC images, equal to 162 images). In all data sets, the number of control and OC images were the same. Thus, TDA using 50 % of experimental data set consisted of 40 control and 40 OC images, both with dimensions of $i = 5$ (number of points on the X axis) × j = 5 (number of points on the Y axis) × k = 8 (number of parameters computed in the time-domain). In FDA and TFDA, k dimensions were 7 and 15 (8 + 7), respectively. To improve the speed of analysis, each image was unfolded as a characteristic vector (Achata et al., 2018). Thereby, each image was reshaped as a vector of i × j × k. As an example, one image in TDA (i = 5 × j = 5 × k = 8) was rearranged from a 3D-matrix to a 1D-row vector of dimension 200. In each approach and dataset, the MIA procedure was followed according to reported by Colucci et al. (2019) and Verdú et al. (2025). The PCA model was employed to extract the latent eigenspace of unfolded control images (without BF). For this purpose, control data sets were randomly split into a segment of 90 % of experimental data for model calibration (C_{cal}). The remaining samples, not included in model training, comprised 10 % of the control data (8 samples) and all OC images (81), which were reserved for external validation. This validation aimed to assess the feasibility of the calibrated PCA model in detecting BF (Reis, 2015). External validation is the gold standard in both supervised and unsupervised data analytics, ensuring generalizability and enhancing confidence in the results (Palacio-Niño & Berzal, 2019). Therefore, for industrial implementation, a larger validation set is recommended to ensure the reliable detection of food contaminants (McGrath et al., 2018; Ten-Doménech et al., 2023).

Firstly, the segment of data for PCA calibration was mean-centered and scaled to have unit variance. The PCA model used the Singular Value Decomposition (SVD) algorithm to extract the orthogonal latent eigenspace by compressing the image information into a LVs. During the scaling process, both the mean and standard deviation vectors obtained from scaling process were saved as PCA control coordinates. Furthermore, the external validation dataset was scaled using the control coordinates and then projected onto the latent space by using the loadings from the control model. The residual sum of squares (RSS) and the Hotelling's T-squared (T^2) multivariate control statistics were computed. The control limit (CL) of both RSS and T^2 were calculated from the values of control images by percentile method considering 90 %, 95 %, 97.5 % and 99 %. Additionally, a limit augmentation (LA) of 0 %, 50 %, 75 % and 100 % was used to increase the decision boundary of computed control limits (Sinisterra-Solís et al., 2024) for exploring its influence in the classification of control and OC images.

2.7. Classification performance and statistical validation

The capability of PCA in the detection of BFs was assessed from 1 LV to the maximal number of LVs in each approach and dataset. Both multivariate control statistics (RSS and T^2) served as the basis to quantify the classification performance of the models by the confusion matrix (CFM, Eq. 19). In this way, the sum of control images from calibration and internal validation dataset with values of RSS and T^2 into the LA-CL indicated true negatives (TN) and if they exceeded the LA-CL, indicated false positives (FP). Regarding the OC images, true positives (TP) involved the OC images which exceeded the LA-CL and were correctly detected. OC images that do not exceed the LA-CL were considered as false negatives (FN). The goodness of classification of each multivariate statistic was assessed by computing figures of merits such as the overall accuracy (A_{cc}, Eq. 20), sensibility (S_e, Eq. 21) and specificity (S_p, Eq. 22) (Craig et al., 2018).

$$\mathrm{CFM} = \begin{array}{c} \\ \text{Predicted} \end{array} \begin{array}{c} \text{Real} \\ \begin{bmatrix} & \text{OC} & \text{UC} \\ \text{OC} & \text{TP} & \text{FP} \\ \text{UC} & \text{FN} & \text{TN} \end{bmatrix} \end{array} \tag{19}$$

$$A_{cc}(\%) = \frac{TP + TN}{TP + TN + FP + FN} * 100 \tag{20}$$

$$S_e = \frac{TP}{TP + FN} \tag{21}$$

$$S_p = \frac{TN}{TN + FP} \tag{22}$$

In order to optimize the PCA model based on RSS and T^2, a multi-objective optimization problem was formulated. The objective function aimed to determine the number of LVs (optimal number of principal components, OPCs) of the PCA model maximizing both the S_e and S_p simultaneously. Thus, the surface response methodology (SRM) and desirability function (D_e) were employed (Kumar et al., 2019; Yolmeh & Jafari, 2017). The optimization processes were carried out using the "fmincon" MATLAB function. All calculations were repeated 100 times to estimate the influence of considering different random partitions of the control matrices to calibrate the PCA model and its influence on the detection of BF. For the selection of the number of LVs of the optimized PCA model in each approach, maximizing the classification performance, a multifactor ANOVA considering the random data partition (as block factor), the CL and their LA and the goodness of classification metrics as responses (A_{cc}, S_e, and S_p) was carried out. All multifactor ANOVA (sections 2.6 and 2.8) were subjected to residual validation (Marques et al., 2020) using different tests on the residuals to assess normality (Shapiro-Wilk's test and q-q plot), independence (Ljung-Box's test), and homoscedasticity (multiple linear regression-MLR on square residuals). Hypothesis tests and fulfillment of statistical assumptions were assessed at a confidence level of 95 %. The statistical analysis was conducted using STATGRAPHICS Centurion XVIII (Manugistics, Inc., Rockville, MD, USA).

3. Results and discussion

3.1. Influence of BF on the ultrasound signals in time and frequency domains

Figs. 3A-3B and 4A-4B-4C show time-domain US signals from the center point (point 13, Fig. 1G) and control (3C) and OC USI (3D-3E, 4D-4E-4F) of chicken breast fillets wherein the different BFs were inserted. Meanwhile, Fig. 5 depicts the phs of control and OC signals also obtained from the center point. A consistent trend was observed in all cases: the BF presence disturbed the time-domain control ultrasound signals and the control frequency-domain spectra. In the case of time-domain, BF of 2.0 × 1.5 cm (Fig. 3A) and 2.0 × 1.0 cm (Fig. 3B) promoted an important decrease in signal amplitude. Moreover, the BF presence led to a pronounced reduction in the maximum peak of the phs (for 2.0 × 1.5 cm, Fig. 5A, and 2.0 × 1.0 cm, Fig. 5B). For BF of 1.5 × 0.3 cm (Fig. 4A-5C), 1.0 × 0.3 cm (Fig. 4B-5D), and 0.5 × 0.3 cm (Fig. 4C-5E), the influence of the BFs led to less pronounced drops in the maximum amplitude of time and frequency-domain signals compared to the samples containing larger size foreign bodies sizes (Correia et al., 2008). Additionally, control USI (Fig. 3C) and all the pixels OC images (control pixels), except point 13, evidenced PP values between 2.8 and 4 V (color bar from orange to yellow), meanwhile for pixels of point 13 in OC images (Fig. 3D-3E and Fig. 4C-4D-4E), PP values ranged between 2 (red) to 0.5 (dark red).

Ultrasound waves are partially scattered, reflected, and transmitted when they are passing through materials with different acoustic impedances (defined as the product of density and velocity), which results in energy attenuation. The attenuation level will be dependent on the

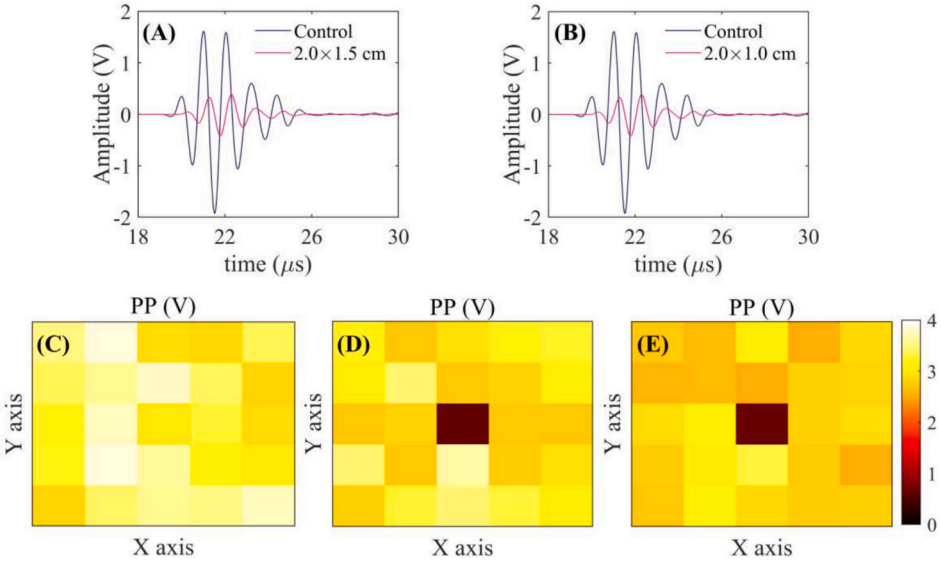

Fig. 3. Ultrasound signals and example of PP (peak-to-peak) images in chicken breast fillets with bone fragments of size 2.0 × 1.5 cm (A, D) and size of 2.0 × 1.0 cm (B, E) placed on its center and control image (C).

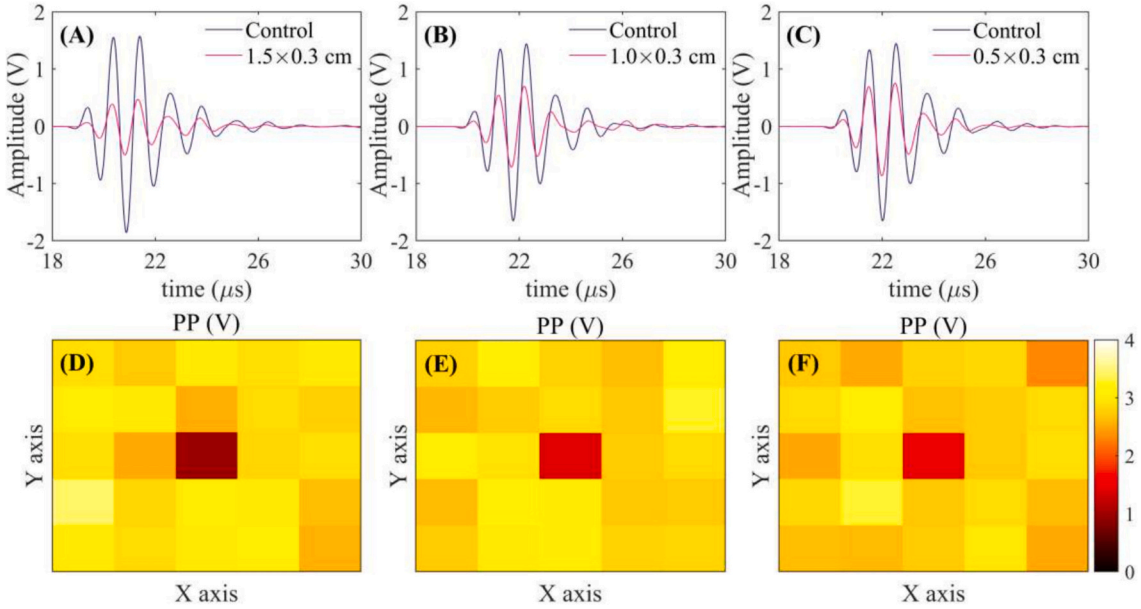

Fig. 4. Ultrasound signals and example of PP (peak-to-peak) images in chicken breast fillets with bone fragments of size 1.5 × 0.3 cm (A, D), size of 1.0 × 0.3 cm (B, E) and size of 0.5 × 0.3 cm (C, F) placed on its center.

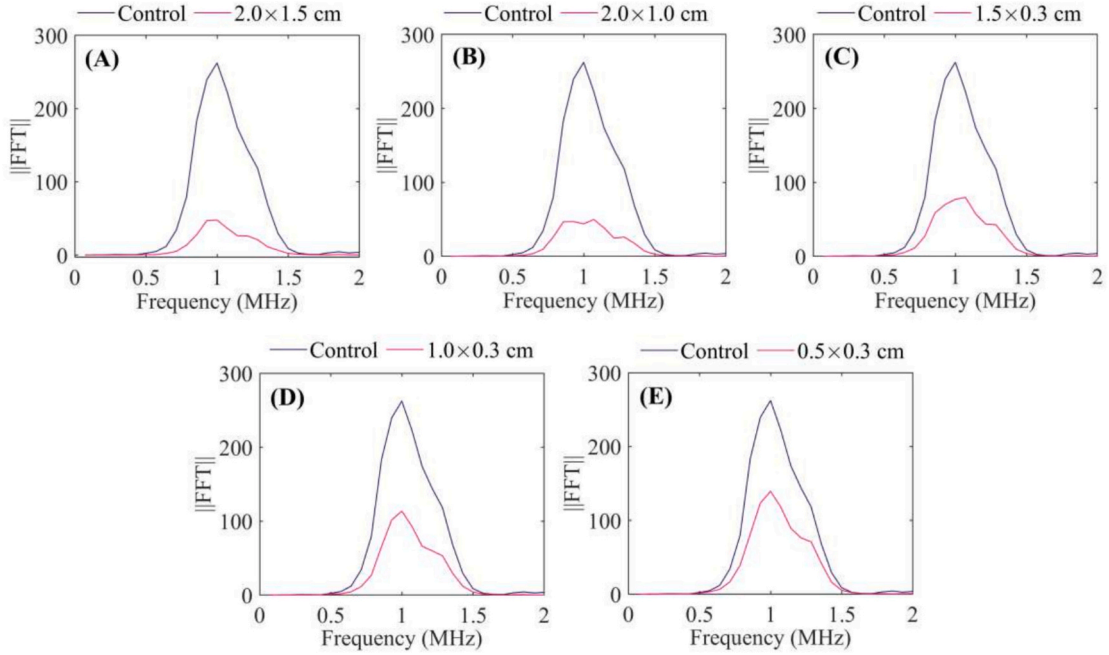

Fig. 5. Example of the frequency spectrum of chicken breast samples with and without bone fragments. Bone fragments of size 2.0 × 1.5 cm (A), size of 2.0 × 1.0 cm (B), size 1.5 × 0.3 cm (C), size of 1.0 × 0.3 cm (D) and size of 0.5 × 0.3 cm (E).

impedance mismatch in the food-foreign bodies interface and the foreign bodies size (Cho & Irudayaraj, 2003). Foreign bodies with gas-filled structures are likely to cause greater energy attenuation due to the significant acoustic impedance mismatch between the gas and the surrounding material (Fariñas, Sanchez-Torres, et al., 2021). Foreign bodies may also cause wave velocity modifications, which will be dependent on the ratios of velocity and thickness between the foreign bodies and the food material (Fariñas et al., 2023).

In order to statistically analyze the abovementioned attenuation effects of BFs within chicken breast samples, a multifactor ANOVA examining the influence of BF size and their location inside the samples, on the energy-related ultrasound parameters computed in the time-frequency domain and ultrasound velocity (section 2.5), was carried out (Tables 1 to 4). Further, the results of the multifactor ANOVA assessed on the L are also shown in Table 1. A statistically significant ($p < 0.05$) effect of the BF size was found on the time and frequency domain ultrasound parameters (Tables 1 to 4). Conversely, the location of the BF did not significantly ($p > 0.05$) affect the ultrasonic parameters, which shows the robustness of the technique to measure the presence of bones of different sizes, regardless of their location. Moreover, the non-statistically significant ($p > 0.05$) effect of BF size or location was found on L (Table 1), which demonstrates that the incorporation of BFs of varying sizes, in different locations, had no impact on the final thickness of the sample, which could have altered the ultrasonic

Table 1
Ultrasound parameters computed in the time-domain (energy-magnitude related and velocity) and thickness for each bone size and location within the sample. Multifactor ANOVA homogeneous groups.

Type	PP (V)	ENG (V^2)	INT (V μs)	V_e (m/s)	L (m)
Position: center (point 13 of the matrix)					
Control	3.8 ± 0.1^{aA}	424.5 ± 3.9^{aA}	204.9 ± 3.5^{aA}	1547.8 ± 11.6^{aA}	0.014 ± 0.002^{aA}
2.0 × 1.5 cm	0.7 ± 0.1^{bA}	11.5 ± 2.3^{bA}	31.0 ± 2.8^{bA}	1433.8 ± 13.0^{bA}	0.016 ± 0.001^{aA}
2.0 × 1.0 cm	0.8 ± 0.1^{bA}	6.9 ± 2.8^{bA}	30.6 ± 1.9^{bA}	1444.9 ± 13.2^{bA}	0.016 ± 0.002^{aA}
1.5 × 0.3 cm	1.1 ± 0.2^{cA}	60.8 ± 2.4^{cA}	66.7 ± 3.6^{cA}	1551.2 ± 7.2^{aA}	0.015 ± 0.001^{aA}
1.0 × 0.3 cm	1.5 ± 0.1^{dA}	59.7 ± 1.8^{cA}	84.4 ± 3.8^{dA}	1552.6 ± 9.1^{aA}	0.016 ± 0.001^{aA}
0.5 × 0.3 cm	1.8 ± 0.2^{eA}	123.2 ± 2.2^{dA}	110.1 ± 2.3^{eA}	1545.9 ± 11.1^{aA}	0.015 ± 0.002^{aA}
Position: top-left (point 7 of the matrix)					
Control	3.8 ± 0.1^{aA}	425.9 ± 2.6^{aA}	202.9 ± 1.9 ^{aA}	1555.2 ± 11.3^{aA}	0.015 ± 0.001^{aA}
2.0 × 1.5 cm	0.6 ± 0.1^{bA}	8.0 ± 3.8^{bA}	31.9 ± 2.9^{bA}	1444.2 ± 11.7^{bA}	0.016 ± 0.001^{aA}
2.0 × 1.0 cm	0.7 ± 0.1^{bA}	9.6 ± 0.5^{bA}	31.0 ± 2.1^{bA}	1445.5 ± 17.0^{bA}	0.015 ± 0.002^{aA}
1.5 × 0.3 cm	0.9 ± 0.1^{cA}	59.9 ± 3.2^{cA}	67.6 ± 7.1^{cA}	1548.4 ± 12.0^{aA}	0.014 ± 0.002^{aA}
1.0 × 0.3 cm	1.5 ± 0.2^{dA}	58.9 ± 3.7^{cA}	84.4 ± 2.6^{dA}	1549.0 ± 12.9^{aA}	0.016 ± 0.001^{aA}
0.5 × 0.3 cm	1.8 ± 0.2^{eA}	120.5 ± 3.4^{dA}	112.5 ± 3.0^{eA}	1536.2 ± 11.1^{aA}	0.015 ± 0.002^{aA}
Position: bottom-left (point 17 of the matrix)					
Control	3.8 ± 0.2^{aA}	424.2 ± 2.8^{aA}	205.6 ± 2.1^{aA}	1546.1 ± 9.5^{aA}	0.017 ± 0.002^{aA}
2.0 × 1.5 cm	0.6 ± 0.2^{bA}	11.3 ± 1.3^{bA}	31.1 ± 4.0^{bA}	1450.4 ± 10.3^{bA}	0.016 ± 0.001^{aA}
2.0 × 1.0 cm	0.7 ± 0.1^{bA}	10.9 ± 1.5^{bA}	30.3 ± 2.8^{bA}	1459.0 ± 9.5^{bA}	0.015 ± 0.002^{aA}
1.5 × 0.3 cm	1.1 ± 0.1^{cA}	59.4 ± 3.3^{cA}	68.1 ± 3.0^{cA}	1534.2 ± 9.0^{aA}	0.014 ± 0.002^{aA}
1.0 × 0.3 cm	1.6 ± 0.1^{dA}	58.3 ± 4.1^{cA}	82.3 ± 2.5^{dA}	1538.1 ± 13.5^{aA}	0.016 ± 0.001^{aA}
0.5 × 0.3 cm	1.9 ± 0.2^{eA}	117.1 ± 2.2^{dA}	113.4 ± 2.2^{eA}	1549.9 ± 11.7^{aA}	0.015 ± 0.002^{aA}
Position: top-right (point 9 of the matrix)					
Control	3.7 ± 0.2^{aA}	427.6 ± 2.9^{aA}	203.3 ± 3.3^{aA}	1551.6 ± 11.2^{aA}	0.014 ± 0.001^{aA}
2.0 × 1.5 cm	0.7 ± 0.1^{bA}	12.5 ± 2.3^{bA}	31.9 ± 4.2^{bA}	1446.5 ± 7.0^{bA}	0.016 ± 0.001^{aA}
2.0 × 1.0 cm	0.7 ± 0.1^{bA}	11.4 ± 1.6^{bA}	28.1 ± 4.7^{bA}	1456.4 ± 7.6^{bA}	0.016 ± 0.001^{aA}
1.5 × 0.3 cm	1.0 ± 0.1^{cA}	57.9 ± 2.5^{cA}	68.0 ± 5.2^{cA}	1543.4 ± 8.6^{aA}	0.016 ± 0.001^{aA}
1.0 × 0.3 cm	1.5 ± 0.1^{dA}	59.6 ± 4.0^{cA}	85.3 ± 3.1^{dA}	1544.8 ± 10.5^{aA}	0.016 ± 0.001^{aA}
0.5 × 0.3 cm	1.8 ± 0.2^{eA}	117.2 ± 1.9^{dA}	114.3 ± 3.1^{eA}	1547.1 ± 8.0^{aA}	0.016 ± 0.001^{aA}
Position: bottom-right (point 19 of the matrix)					
Control	3.7 ± 0.2^{aA}	429.2 ± 2.2^{aA}	202.3 ± 2.1^{aA}	1548.2 ± 8.1^{aA}	0.015 ± 0.002^{aA}
2.0 × 1.5 cm	0.6 ± 0.1^{bA}	11.5 ± 2.4^{bA}	29.8 ± 2.4^{bA}	1434.0 ± 10.6^{bA}	0.016 ± 0.002^{aA}
2.0 × 1.0 cm	0.7 ± 0.2^{bA}	11.5 ± 1.3^{bA}	30.2 ± 2.6^{bA}	1437.4 ± 11.0^{bA}	0.014 ± 0.002^{aA}
1.5 × 0.3 cm	1.0 ± 0.1^{cA}	57.1 ± 3.4^{cA}	67.9 ± 4.6^{cA}	1540.1 ± 11.3^{aA}	0.016 ± 0.001^{aA}
1.0 × 0.3 cm	1.5 ± 0.2^{dA}	57.8 ± 2.8^{cA}	86.4 ± 4.6^{dA}	1540.7 ± 12.1^{aA}	0.015 ± 0.002^{aA}
0.5 × 0.3 cm	1.9 ± 0.1^{eA}	123.3 ± 2.3^{dA}	114.6 ± 2.6^{eA}	1549.2 ± 8.0^{aA}	0.016 ± 0.001^{aA}

PP (peak-to-peak), ENG (energy), INT (integral), V_e (ultrasound velocity), and L (thickness). Results are expressed as mean ± standard error. Different lowercase letters indicate statistically significant differences (95 %) for each ultrasound parameter as a function of the size of bone fragments. Uppercase letters indicate statistically significant differences (95 %) for the location of these bone pieces within the chicken breast.

Table 2
Ultrasound parameters computed in the time-domain (energy-distribution) for each bone size and location within the sample. Multifactor ANOVA homogeneous groups.

Type	VAR_t (V^2)	SKE_t	KUR_t	ENT_t
Position: center (point 13 of the matrix)				
Control	$0.34 \pm 6 \times 10^{-3aA}$	$-0.11 \pm 9 \times 10^{-3aA}$	8.92 ± 0.06^{aA}	3.3 ± 0.1^{aA}
2.0 × 1.5 cm	$7 \times 10^{-3} \pm 1 \times 10^{-3bA}$	$0.10 \pm 7 \times 10^{-3bA}$	8.03 ± 0.07^{bA}	2.1 ± 0.1^{bA}
2.0 × 1.0 cm	$8 \times 10^{-3} \pm 1 \times 10^{-3bA}$	$0.11 \pm 8 \times 10^{-3bA}$	8.12 ± 0.06^{bA}	2.1 ± 0.1^{bA}
1.5 × 0.3 cm	$0.04 \pm 6 \times 10^{-3cA}$	$-0.03 \pm 8 \times 10^{-3cA}$	8.21 ± 0.07^{cA}	2.4 ± 0.1^{cA}
1.0 × 0.3 cm	$0.07 \pm 3 \times 10^{-3dA}$	$-0.03 \pm 8 \times 10^{-3cA}$	8.30 ± 0.07^{dA}	2.6 ± 0.2^{dA}
0.5 × 0.3 cm	$0.10 \pm 6 \times 10^{-3eA}$	$-0.06 \pm 6 \times 10^{-3dA}$	8.52 ± 0.07^{eA}	2.7 ± 0.1^{eA}
Position: top-left (point 7 of the matrix)				
Control	$0.34 \pm 8 \times 10^{-3aA}$	$-0.12 \pm 6 \times 10^{-3aA}$	8.84 ± 0.06^{aA}	3.3 ± 0.1^{aA}
2.0 × 1.5 cm	$7 \times 10^{-3} \pm 2 \times 10^{-3bA}$	$0.10 \pm 8 \times 10^{-3bA}$	8.06 ± 0.06^{bA}	2.1 ± 0.1^{bA}
2.0 × 1.0 cm	$9 \times 10^{-3} \pm 1 \times 10^{-3bA}$	$0.10 \pm 7 \times 10^{-3bA}$	8.06 ± 0.06^{bA}	2.1 ± 0.1^{bA}
1.5 × 0.3 cm	$0.04 \pm 8 \times 10^{-3cA}$	$-0.03 \pm 5 \times 10^{-3cA}$	8.19 ± 0.05^{cA}	2.4 ± 0.1^{cA}
1.0 × 0.3 cm	$0.08 \pm 2 \times 10^{-3dA}$	$-0.03 \pm 6 \times 10^{-3cA}$	8.29 ± 0.08^{dA}	2.6 ± 0.1^{dA}
0.5 × 0.3 cm	$0.10 \pm 7 \times 10^{-3eA}$	$-0.07 \pm 8 \times 10^{-3dA}$	8.55 ± 0.07^{eA}	2.7 ± 0.1^{eA}
Position: bottom-left (point 17 of the matrix)				
Control	$0.34 \pm 7 \times 10^{-3aA}$	$-0.11 \pm 6 \times 10^{-3aA}$	8.87 ± 0.05^{aA}	3.2 ± 0.1^{aA}
2.0 × 1.5 cm	$7 \times 10^{-3} \pm 1 \times 10^{-3bA}$	$0.10 \pm 7 \times 10^{-3bA}$	8.08 ± 0.06^{bA}	2.1 ± 0.1^{bA}
2.0 × 1.0 cm	$8 \times 10^{-3} \pm 1 \times 10^{-3bA}$	$0.10 \pm 6 \times 10^{-3bA}$	8.05 ± 0.05^{bA}	2.1 ± 0.1^{bA}
1.5 × 0.3 cm	$0.04 \pm 6 \times 10^{-3cA}$	$-0.04 \pm 7 \times 10^{-3cA}$	8.24 ± 0.07^{cA}	2.5 ± 0.1^{cA}
1.0 × 0.3 cm	$0.08 \pm 3 \times 10^{-3dA}$	$-0.05 \pm 6 \times 10^{-3cA}$	8.33 ± 0.06^{dA}	2.6 ± 0.1^{dA}
0.5 × 0.3 cm	$0.10 \pm 7 \times 10^{-3eA}$	$-0.07 \pm 6 \times 10^{-3dA}$	8.56 ± 0.06^{eA}	2.7 ± 0.1^{eA}
Position: top-right (point 9 of the matrix)				
Control	$0.33 \pm 5 \times 10^{-3aA}$	$-0.11 \pm 8 \times 10^{-3aA}$	8.92 ± 0.08^{aA}	3.2 ± 0.1^{aA}
2.0 × 1.5 cm	$7 \times 10^{-3} \pm 1 \times 10^{-3bA}$	$0.10 \pm 7 \times 10^{-3bA}$	8.06 ± 0.07^{bA}	2.1 ± 0.1^{bA}
2.0 × 1.0 cm	$8 \times 10^{-3} \pm 1 \times 10^{-3bA}$	$0.10 \pm 7 \times 10^{-3bA}$	8.14 ± 0.08^{bA}	2.2 ± 0.1^{bA}
1.5 × 0.3 cm	$0.04 \pm 5 \times 10^{-3cA}$	$-0.03 \pm 5 \times 10^{-3cA}$	8.23 ± 0.07^{cA}	2.4 ± 0.1^{cA}
1.0 × 0.3 cm	$0.08 \pm 4 \times 10^{-3dA}$	$-0.03 \pm 5 \times 10^{-3cA}$	8.32 ± 0.07^{dA}	2.6 ± 0.1^{dA}
0.5 × 0.3 cm	$0.10 \pm 8 \times 10^{-3eA}$	$-0.06 \pm 5 \times 10^{-3dA}$	8.54 ± 0.05^{eA}	2.7 ± 0.1^{eA}
Position: bottom-right (point 19 of the matrix)				
Control	$0.34 \pm 8 \times 10^{-3aA}$	$-0.11 \pm 8 \times 10^{-3aA}$	8.91 ± 0.05^{aA}	3.2 ± 0.1^{aA}
2.0 × 1.5 cm	$7 \times 10^{-3} \pm 1 \times 10^{-3bA}$	$0.10 \pm 8 \times 10^{-3bA}$	8.07 ± 0.07^{bA}	2.1 ± 0.1^{bA}
2.0 × 1.0 cm	$8 \times 10^{-3} \pm 1 \times 10^{-3bA}$	$0.11 \pm 6 \times 10^{-3bA}$	8.16 ± 0.05^{bA}	2.1 ± 0.1^{bA}
1.5 × 0.3 cm	$0.04 \pm 4 \times 10^{-3cA}$	$-0.03 \pm 5 \times 10^{-3cA}$	8.21 ± 0.06^{cA}	2.4 ± 0.1^{cA}
1.0 × 0.3 cm	$0.07 \pm 3 \times 10^{-3dA}$	$-0.03 \pm 6 \times 10^{-3cA}$	8.33 ± 0.06^{dA}	2.5 ± 0.1^{dA}
0.5 × 0.3 cm	$0.10 \pm 7 \times 10^{-3eA}$	$-0.07 \pm 5 \times 10^{-3dA}$	8.54 ± 0.06^{eA}	2.7 ± 0.1^{eA}

VAR_t (variance in time-domain), SKE_t (skewness in time-domain), KUR_t (kurtosis in time-domain) and ENT_t (entropy in time-domain). Results are expressed as mean ± standard error. Different lowercase letters indicate statistically significant differences (95 %) for each ultrasound parameter as a function of the size of bone fragments. Uppercase letters indicate statistically significant differences (95 %) for the location of these bone pieces within the chicken breast.

Table 3
Ultrasound parameters computed in the frequency-domain (energy-magnitude related) for each bone size and location within the sample. Multifactor ANOVA homogeneous groups.

Position: center (point 13 of the matrix)			
Type	M_0 (MHz)	F_r	MP
Control	2177.8 ± 64.6^{aA}	1.00 ± 0.01^{aA}	296.2 ± 16.9^{aA}
2.0 × 1.5 cm	396.1 ± 64.6^{bA}	1.02 ± 0.01^{bA}	42.7 ± 3.7^{bA}
2.0 × 1.0 cm	333.7 ± 59.4^{bA}	1.03 ± 0.01^{bcA}	43.1 ± 5.7^{bA}
1.5 × 0.3 cm	770.1 ± 62.9^{cA}	1.03 ± 0.02^{bcA}	89.8 ± 6.7^{cA}
1.0 × 0.3 cm	787.5 ± 73.5^{cA}	1.02 ± 0.01^{bcA}	98.0 ± 6.6^{cA}
0.5 × 0.3 cm	827.7 ± 62.4^{cA}	1.03 ± 0.01^{cA}	103.4 ± 11.3^{cA}
Position: top-left (point 7 of the matrix)			
Control	2094.8 ± 65.9^{aA}	1.00 ± 0.01^{aA}	297.0 ± 8.3^{aA}
2.0 × 1.5 cm	354.3 ± 56.3^{bA}	1.02 ± 0.01^{bA}	41.4 ± 5.5^{bA}
2.0 × 1.0 cm	383.0 ± 67.7^{bA}	1.02 ± 0.00^{bcA}	46.7 ± 10.1^{bA}
1.5 × 0.3 cm	791.6 ± 63.4^{cA}	1.02 ± 0.01^{bcA}	89.1 ± 7.5^{cA}
1.0 × 0.3 cm	831.5 ± 65.3^{cA}	1.03 ± 0.01^{bcA}	89.4 ± 10.6^{cA}
0.5 × 0.3 cm	862.9 ± 71.2^{cA}	1.03 ± 0.01^{cA}	94.5 ± 14.5^{cA}
Position: bottom-left (point 17 of the matrix)			
Control	2164.4 ± 62.7^{aA}	1.01 ± 0.01^{aA}	294.1 ± 14.0^{aA}
2.0 × 1.5 cm	393.6 ± 49.2^{bA}	1.02 ± 0.01^{bA}	35.5 ± 8.4^{bA}
2.0 × 1.0 cm	395.0 ± 67.6^{bA}	1.02 ± 0.01^{bcA}	46.8 ± 8.1^{bA}
1.5 × 0.3 cm	805.2 ± 68.6^{cA}	1.03 ± 0.01^{bcA}	87.2 ± 14.0^{cA}
1.0 × 0.3 cm	785.8 ± 57.8^{cA}	1.02 ± 0.02^{bcA}	95.2 ± 14.3^{cA}
0.5 × 0.3 cm	851.9 ± 61.2^{cA}	1.03 ± 0.00^{cA}	103.7 ± 11.3^{cA}
Position: top-right (point 9 of the matrix)			
Control	2116.5 ± 61.9^{aA}	1.00 ± 0.01^{aA}	295.7 ± 8.1^{aA}
2.0 × 1.5 cm	376.6 ± 54.8^{bA}	1.02 ± 0.01^{bA}	38.9 ± 8.1^{bA}
2.0 × 1.0 cm	379.8 ± 49.2^{bA}	1.03 ± 0.02^{bcA}	47.0 ± 8.4^{bA}
1.5 × 0.3 cm	757.9 ± 67.2^{cA}	1.02 ± 0.02^{bcA}	93.6 ± 8.1^{cA}
1.0 × 0.3 cm	816.1 ± 55.1^{cA}	1.03 ± 0.01^{bcA}	97.9 ± 8.1^{cA}
0.5 × 0.3 cm	835.1 ± 60.7^{cA}	1.03 ± 0.02^{cA}	108.4 ± 8.4^{cA}
Position: bottom-right (point 19 of the matrix)			
Control	2057.9 ± 71.7^{aA}	1.00 ± 0.01^{aA}	298.3 ± 2.5^{aA}
2.0 × 1.5 cm	305.9 ± 58.8^{bA}	1.02 ± 0.00^{bA}	33.5 ± 6.4^{bA}
2.0 × 1.0 cm	314.9 ± 58.9^{bA}	1.04 ± 0.01^{bcA}	40.4 ± 4.1^{bA}
1.5 × 0.3 cm	733.9 ± 57.6^{cA}	1.02 ± 0.01^{bcA}	90.7 ± 4.8^{cA}
1.0 × 0.3 cm	782.2 ± 67.7^{cA}	1.03 ± 0.01^{bcA}	92.8 ± 7.3^{cA}
0.5 × 0.3 cm	798.5 ± 67.4^{cA}	1.02 ± 0.01^{cA}	96.5 ± 5.8^{cA}

M_0 (zero-order moment), F_r (center frequency), and MP (maximum peak of the frequency spectrum). Results are expressed as mean ± standard error. Different lowercase letters indicate statistically significant differences (95 %) for each ultrasound parameter as a function of the size of bone fragments. Uppercase letters indicate statistically significant differences (95 %) for the location of these bone pieces within the chicken breast.

Table 4
Ultrasound parameters computed in the frequency-domain (energy-distribution) for each bone size and location within the sample. Multifactor ANOVA homogeneous groups.

Position: center (point 13 of the matrix)				
Type	VAR_{sp}	SKE_{sp}	KUR_{sp}	ENT_{sp}
Control	6782.2 ± 68.2^{aA}	1.45 ± 0.02^{aA}	3.7 ± 0.1^{aA}	0.5 ± 0.1^{aA}
2.0 × 1.5 cm	160.4 ± 42.8^{bA}	1.29 ± 0.07^{bcA}	3.3 ± 0.3^{bcA}	2.8 ± 0.2^{bA}
2.0 × 1.0 cm	166.4 ± 56.8^{bA}	1.36 ± 0.05^{bA}	3.2 ± 0.1^{bA}	2.7 ± 0.2^{bA}
1.5 × 0.3 cm	954.8 ± 75.3^{cA}	1.35 ± 0.17^{cA}	3.5 ± 0.1^{cA}	2.3 ± 0.1^{cA}
1.0 × 0.3 cm	1776.8 ± 88.7^{dA}	1.35 ± 0.06^{bcA}	3.3 ± 0.2^{bcA}	2.3 ± 0.1^{cA}
0.5 × 0.3 cm	1884.7 ± 75.5^{dA}	1.31 ± 0.03^{bcA}	3.2 ± 0.1^{bcA}	2.2 ± 0.1^{cA}
Position: top-left (point 7 of the matrix)				
Control	6769.8 ± 69.2^{aA}	1.45 ± 0.03^{aA}	3.7 ± 0.1^{aA}	0.3 ± 0.1^{aA}
2.0 × 1.5 cm	107.1 ± 53.9^{bA}	1.32 ± 0.21^{bcA}	3.4 ± 0.2^{bcA}	2.9 ± 0.1^{bA}
2.0 × 1.0 cm	120.6 ± 42.6^{bA}	1.25 ± 0.2^{bA}	3.1 ± 0.3^{bA}	2.9 ± 0.2^{bA}
1.5 × 0.3 cm	955.3 ± 76.2^{cA}	1.38 ± 0.09^{cA}	3.5 ± 0.3^{cA}	2.4 ± 0.2^{cA}
1.0 × 0.3 cm	1715.3 ± 64.0^{dA}	1.32 ± 0.15^{bcA}	3.3 ± 0.4^{bcA}	2.4 ± 0.1^{cA}
0.5 × 0.3 cm	1895.1 ± 77.7^{dA}	1.38 ± 0.03^{bcA}	3.5 ± 0.1^{bcA}	2.5 ± 0.1^{cA}
Position: bottom-left (point 17 of the matrix)				
Control	6776.9 ± 62.2^{aA}	1.43 ± 0.03^{aA}	3.6 ± 0.1^{aA}	0.4 ± 0.1^{aA}
2.0 × 1.5 cm	100.3 ± 45.3^{bA}	1.35 ± 0.11^{bcA}	3.3 ± 0.2^{bcA}	2.9 ± 0.1^{bA}
2.0 × 1.0 cm	129.1 ± 47.1^{bA}	1.36 ± 0.10^{bA}	3.2 ± 0.4^{bA}	2.8 ± 0.1^{bA}
1.5 × 0.3 cm	898.9 ± 69.2^{cA}	1.42 ± 0.02^{cA}	3.3 ± 0.1^{cA}	2.5 ± 0.1^{cA}
1.0 × 0.3 cm	1726.4 ± 58.9^{dA}	1.37 ± 0.12^{bcA}	3.2 ± 0.2^{bcA}	2.4 ± 0.2^{cA}
0.5 × 0.3 cm	1886.2 ± 54.6^{dA}	1.38 ± 0.03^{bcA}	3.3 ± 0.1^{bcA}	2.5 ± 0.2^{cA}
Position: top-right (point 9 of the matrix)				
Control	6746.8 ± 77.7^{aA}	1.45 ± 0.03^{aA}	3.7 ± 0.1^{aA}	0.6 ± 0.2^{aA}
2.0 × 1.5 cm	122.6 ± 42.6^{bA}	1.30 ± 0.12^{bcA}	3.2 ± 0.2^{bcA}	3.0 ± 0.2^{bA}
2.0 × 1.0 cm	138.7 ± 56.8^{bA}	1.25 ± 0.12^{bA}	3.1 ± 0.2^{bA}	2.9 ± 0.1^{bA}
1.5 × 0.3 cm	931.0 ± 65.3^{cA}	1.36 ± 0.09^{cA}	3.2 ± 0.1^{cA}	2.4 ± 0.1^{cA}
1.0 × 0.3 cm	1712.3 ± 78.7^{dA}	1.32 ± 0.03^{bcA}	3.2 ± 0.2^{bcA}	2.5 ± 0.1^{cA}
0.5 × 0.3 cm	1890.3 ± 51.9^{dA}	1.34 ± 0.06^{bcA}	3.0 ± 0.2^{bcA}	2.5 ± 0.2^{cA}
Position: bottom-right (point 19 of the matrix)				
Control	6795.3 ± 67.6^{aA}	1.45 ± 0.02^{aA}	3.7 ± 0.1^{aA}	0.4 ± 0.2^{aA}
2.0 × 1.5 cm	128.0 ± 38.8^{bA}	1.33 ± 0.08^{bcA}	3.2 ± 0.3^{bcA}	2.9 ± 0.1^{bA}
2.0 × 1.0 cm	141.6 ± 36.8^{bA}	1.28 ± 0.05^{bA}	3.1 ± 0.2^{bA}	3.0 ± 0.1^{bA}
1.5 × 0.3 cm	888.5 ± 40.6^{cA}	1.32 ± 0.05^{cA}	3.2 ± 0.2^{cA}	2.4 ± 0.1^{cA}
1.0 × 0.3 cm	1722.1 ± 59.0^{dA}	1.37 ± 0.10^{bcA}	3.3 ± 0.2^{bcA}	2.4 ± 0.2^{cA}
0.5 × 0.3 cm	1840.2 ± 47.6^{dA}	1.39 ± 0.02^{bcA}	3.7 ± 0.1^{bcA}	2.5 ± 0.2^{cA}

VAR_{sp} (spectral-variance), SKE_{sp} (spectral-skewness), KUR_{sp} (spectral-kurtosis) and ENT_{sp} (spectral-entropy). Results are expressed as mean ± standard error. Different lowercase letters indicate statistically significant differences (95 %) for each ultrasound parameter as a function of the size of bone fragments. Uppercase letters indicate statistically significant differences (95 %) for the location of these bone pieces within the chicken breast.

measurements.

By using the average values of PP, ENG and INT computed from time-domain (Table 1), it was possible to sort the samples from the lowest to the highest energy level in five homogeneous groups (LSD intervals ($p < 0.05$) from ANOVA), as follows: control (3.8 V, 424.5 V^2 and 204.9 V μs) > 0.5 × 0.3 cm (1.8 V, 123.2 V^2 and 110.1 V μs) > 1.0 × 0.3 cm (1.5 V, 59.7 V^2 and 84.4 V μs) > 1.5 × 0.3 cm (1.1 V, 60.8 V^2 and 66.7 V μs), 2.0 × 1.0 cm (0.8 V, 6.9 V^2 and 30.6 V μs) > 2.0 × 1.5 cm (0.7 V, 11.5 V^2 and 31 V μs). Thus, the larger the BF, the lower the energy level and then, the larger the attenuation. In addition, the statistical results for V_e indicated that there were no significant differences ($p > 0.05$) in the speed of ultrasound waves between the control group and BFs of sizes 1.5 × 0.3 cm, 1.0 × 0.3 cm, and 0.5 × 0.3 cm. However, a noticeable decrease in the ultrasound velocity was found for the largest BF sizes (2.0 × 1.5 cm and 2.0 × 1.0 cm, Table 1). These results suggest that for small bones the wave front (used to calculate velocity) travels only through the meat flesh (where velocity is higher) and therefore velocity is not altered, compared to the control sample. However, when the bone size is larger, the wave front has traveled through the bone (with lower ultrasound velocity than flesh) and therefore ultrasonic velocity decreases. Similar results were reported by Correia et al. (2008) in the detection of BFs of different sizes (large size = 15.75 mm^2, medium size = 9.92 mm^2 and small size = 6.18 mm^2) inserted in skinless chicken breasts by using a single point-measurement using pulse-eco ultrasound technology. These authors quantified the influence of these BFs on both the amplitude ratio and V_e. They found that the presence of BF led to a statistically significant ($p < 0.05$) increase in ultrasonic attenuation, while non statistical differences ($p > 0.05$) were found in V_e. This study reported V_e values of 1564 ± 2 m/s for chicken breast samples, similar to the values of the present work (Table 1). Although Correia et al. (2008) claimed that the V_e could not be used to detect the presence of BFs, the results of the present work illustrate that the largest BFs, which were obtained from other parts of the chicken skeleton such as vertebra (2.0 × 1.5 cm, Fig. 1E i) and chest (2.0 × 1.0 cm, Fig. 1E ii), were detected by using V_e.

The presence of BF also influenced the energy-distribution parameters calculated from time-domain (VARt, SKEt, KURt and ENTt, Table 2). Larger BF led to a decrease in the dispersion of the ultrasound waves (VARt), left-skewed the time-domain signals (positive SKEt values), reduced the tailedness (KURt) and the randomness (ENTt). Thus, a noticeable trend was observed from the energy time-domain distribution, the larger the BFs, the most pronounced changes in the energy-distribution of the ultrasound signals waves.

As regard of the energy-magnitude related variables computed in the frequency-domain (M_0, F_r and MP, Table 3), the BF presence within chicken breast samples significantly ($p < 0.05$) reduced M_0 and MP (Fig. 5) and also modified the center-frequency of phs (F_r). Multifactor ANOVA of M_0 and MP, showed three independent groups clustered from LSD intervals: i) Control ii) BF of 1.5 × 0.3 cm, 1.0 × 0.3 cm and 0.5 ×

0.3 cm iii) BF of 2.0 × 1.5 cm and 2.0 × 1.0 cm. While the results of F_r led to also discriminate three groups (Table 3). BF presence also influenced the phs energy-distribution. Large BF produced an important decrease in the dispersion of phs (VAR_{sp}), right-skewed (positive SKE_{sp} values but smaller than control), reduced the tailedness and increased the disorder in the distribution of energy of phs (ENT_{sp}). Therefore, the frequency-domain energy-magnitude and distribution parameters were also adequate to detect the presence of BFs in the breasts.

3.2. BF detection using USI and latent-based statistical process control

The statistical results considering the USI for the detection of BFs by using the RSS and T^2 and the TDA, FDA and TFDA approaches (section 2.7.1 and 2.8), are summarized in Tables 5 to 8. The modeling results (Tables 5, 6 and 7) reported that the average values of A_{cc} ranged between 88.2 and 96.07 %, S_e were between 0.88 and 0.96 and S_p varied from 0.88 to 0.96, for TDA, FDA and TFDA in all CL of both RSS and T^2 and their LA. This demonstrates the noteworthy performance of this approach for detecting BFs using both multivariate control charts (RSS and T^2) computed in the MIA-based strategy.

The statistical results of multifactor ANOVA models computed from TDA, FDA and TFDA revealed significant differences ($p < 0.05$) in the average A_{cc} S_e and S_p values of the optimized PCA models by using

Table 5
Optimized Principal Component models (PCA) and statistical performance of the Residual Sum Squares (RSS) and Hotelling's T-squared (T^2) multivariate control statistics for detection of bone fragments using time-domain approach (TDA).

TDA-RSS					
LA (%)	CL (%)	OPCs	A_{cc} (%)	S_e	S_p
0	90	6	89.00 ± 0.84^{aA}	0.90 ± 0.02^{aA}	0.88 ± 0.02^{aA}
	95	8	91.61 ± 0.81^{aB}	0.92 ± 0.01^{aB}	0.91 ± 0.02^{aB}
	97.5	12	93.90 ± 0.85^{aC}	0.94 ± 0.02^{aC}	0.94 ± 0.02^{aC}
	99	14	94.25 ± 1.04^{aC}	0.94 ± 0.03^{aC}	0.95 ± 0.02^{aC}
50	**90**	**17**	**95.44 ± 0.90^{bA}**	**0.96 ± 0.01^{bA}**	**0.95 ± 0.02^{bA}**
	95	19	95.49 ± 0.82^{bA}	0.96 ± 0.02^{bA}	0.95 ± 0.02^{bA}
	97.5	21	95.75 ± 0.82^{bA}	0.96 ± 0.01^{bA}	0.96 ± 0.02^{bA}
	99	23	95.67 ± 0.95^{bA}	0.96 ± 0.01^{bA}	0.96 ± 0.02^{bA}
75	90	20	95.61 ± 0.84^{bA}	0.95 ± 0.01^{bA}	0.96 ± 0.02^{bA}
	95	23	95.60 ± 0.83^{bA}	0.96 ± 0.01^{bA}	0.95 ± 0.02^{bA}
	97.5	25	95.78 ± 0.81^{bA}	0.96 ± 0.02^{bA}	0.96 ± 0.02^{bA}
	99	27	95.90 ± 0.92^{bB}	0.96 ± 0.02^{bA}	0.96 ± 0.02^{bA}
100	90	23	95.72 ± 0.79^{bA}	0.96 ± 0.01^{bA}	0.96 ± 0.02^{bA}
	95	25	95.53 ± 0.80^{bA}	0.96 ± 0.02^{bA}	0.96 ± 0.02^{bA}
	97.5	26	95.19 ± 0.74^{bA}	0.95 ± 0.02^{bA}	0.96 ± 0.02^{bA}
	99	28	95.55 ± 1.05^{bA}	0.95 ± 0.02^{bA}	0.96 ± 0.02^{bA}
TDA-T^2					
LA (%)	CL (%)	OPCs	A_{cc} (%)	S_e	S_p
0	90	42	88.20 ± 1.10^{aA}	0.88 ± 0.02^{aA}	0.88 ± 0.02^{aA}
	95	45	91.40 ± 1.04^{aB}	0.92 ± 0.02^{aB}	0.91 ± 0.02^{aB}
	97.5	47	93.38 ± 0.91^{aC}	0.94 ± 0.02^{aC}	0.93 ± 0.02^{aC}
	99	48	94.48 ± 1.01^{aD}	0.95 ± 0.02^{aD}	0.94 ± 0.02^{aC}
50	90	54	94.89 ± 0.97^{bA}	0.94 ± 0.02^{bA}	0.95 ± 0.02^{bA}
	95	**55**	**95.38 ± 1.01^{bB}**	**0.96 ± 0.02^{bA}**	**0.95 ± 0.02^{bA}**
	97.5	55	95.40 ± 0.99^{bB}	0.96 ± 0.02^{bA}	0.95 ± 0.02^{bA}
	99	55	95.38 ± 1.00^{bB}	0.96 ± 0.02^{bA}	0.95 ± 0.02^{bA}
75	90	57	95.20 ± 1.02^{cA}	0.96 ± 0.02^{bA}	0.95 ± 0.02^{bA}
	95	57	95.18 ± 1.01^{cA}	0.96 ± 0.02^{bA}	0.95 ± 0.02^{bA}
	97.5	57	95.17 ± 1.00^{cA}	0.96 ± 0.02^{bA}	0.95 ± 0.02^{bA}
	99	57	95.14 ± 0.99^{cA}	0.96 ± 0.02^{bA}	0.95 ± 0.02^{bA}
100	90	58	94.94 ± 1.00^{bcA}	0.95 ± 0.02^{bA}	0.95 ± 0.02^{bA}
	95	58	94.93 ± 1.00^{bcA}	0.94 ± 0.02^{bA}	0.95 ± 0.02^{bA}
	97.5	58	94.93 ± 0.99^{bcA}	0.94 ± 0.02^{bA}	0.95 ± 0.02^{bA}
	99	58	94.92 ± 0.98^{bcA}	0.94 ± 0.02^{bA}	0.95 ± 0.02^{bA}

TDA (time-domain approach), RSS (Residual Sum Squares), T^2 (Hotelling T-squared), LA (limit augmentation), CL (control limit), OPCs (optimal number of principal components), A_{cc} (overall accuracy), S_e (sensibility) and S_p (specificity). Results are expressed as mean ± standard error. Different lowercase letters indicate statistically significant differences (95 %) of each goodness of classification metric (A_{cc}, S_e and S_p) as a function of the LA. Uppercase letters indicate statistically significant differences (95 %) of A_{cc}, S_e and S_p as a function of the computed CL.

Table 6
Optimized Principal Component models (PCA) and statistical performance of the Residual Sum Squares (RSS) and Hotelling's T-squared (T^2) multivariate control statistics for detection of bone fragments using frequency-domain approach (FDA).

FDA-RSS					
LA (%)	CL (%)	OPCs	A_{cc} (%)	S_e	S_p
0	90	6	89.31 ± 1.23^{aA}	0.90 ± 0.04^{aA}	0.88 ± 0.02^{aA}
	95	8	91.75 ± 0.84^{aB}	0.92 ± 0.01^{aA}	0.91 ± 0.02^{aB}
	97.5	10	93.35 ± 1.13^{aB}	0.93 ± 0.03^{aA}	0.94 ± 0.02^{aC}
	99	12	95.40 ± 1.10^{aC}	0.96 ± 0.02^{aB}	0.95 ± 0.02^{aC}
50	90	15	95.44 ± 0.96^{bA}	0.95 ± 0.02^{bA}	0.96 ± 0.02^{bA}
	95	**17**	**95.83 ± 0.98^{bA}**	**0.96 ± 0.02^{bAB}**	**0.96 ± 0.02^{bA}**
	97.5	19	95.85 ± 0.95^{bA}	0.96 ± 0.01^{bB}	0.96 ± 0.02^{bA}
	99	20	95.63 ± 0.99^{bA}	0.96 ± 0.02^{bB}	0.96 ± 0.02^{bA}
75	90	18	95.84 ± 0.91^{bA}	0.96 ± 0.01^{bA}	0.96 ± 0.02^{bA}
	95	20	95.80 ± 0.84^{bA}	0.95 ± 0.02^{bA}	0.96 ± 0.02^{bA}
	97.5	21	95.44 ± 0.92^{bA}	0.95 ± 0.02^{bA}	0.96 ± 0.02^{bA}
	99	23	95.77 ± 0.81^{bA}	0.96 ± 0.01^{bA}	0.95 ± 0.02^{bA}
100	90	21	95.72 ± 0.84^{bA}	0.96 ± 0.01^{bA}	0.96 ± 0.02^{bA}
	95	23	95.93 ± 0.73^{bA}	0.96 ± 0.01^{bA}	0.96 ± 0.02^{bA}
	97.5	24	95.74 ± 0.90^{bA}	0.96 ± 0.02^{bA}	0.96 ± 0.02^{bA}
	99	25	95.61 ± 0.81^{bA}	0.96 ± 0.02^{bA}	0.96 ± 0.02^{bA}
FDA-T^2					
LA (%)	CL (%)	OPCs	A_{cc} (%)	S_e	S_p
0	90	41	88.07 ± 1.32^{aA}	0.88 ± 0.03^{aA}	0.88 ± 0.02^{aA}
	95	43	91.35 ± 1.36^{aB}	0.91 ± 0.03^{aB}	0.92 ± 0.02^{aB}
	97.5	45	93.67 ± 1.17^{aC}	0.94 ± 0.02^{aC}	0.94 ± 0.02^{aC}
	99	46	94.94 ± 0.92^{aD}	0.95 ± 0.02^{aC}	0.95 ± 0.02^{aC}
50	90	55	95.49 ± 0.88^{bA}	0.96 ± 0.02^{bA}	0.95 ± 0.02^{bA}
	95	**55**	**95.44 ± 0.85^{bA}**	**0.95 ± 0.02^{bA}**	**0.95 ± 0.02^{bA}**
	97.5	55	95.44 ± 0.84^{bA}	0.95 ± 0.02^{bA}	0.95 ± 0.02^{bA}
	99	55	95.41 ± 0.83^{bA}	0.95 ± 0.02^{bA}	0.95 ± 0.02^{bA}
75	90	57	95.30 ± 0.90^{bA}	0.95 ± 0.02^{bA}	0.95 ± 0.02^{bA}
	95	57	95.25 ± 0.91^{bA}	0.95 ± 0.02^{bA}	0.95 ± 0.02^{bA}
	97.5	57	95.25 ± 0.91^{bA}	0.95 ± 0.02^{bA}	0.95 ± 0.02^{bA}
	99	57	95.24 ± 0.91^{bA}	0.95 ± 0.02^{bA}	0.95 ± 0.02^{bA}
100	90	59	95.29 ± 0.96^{bA}	0.95 ± 0.02^{bA}	0.95 ± 0.02^{bA}
	95	59	95.30 ± 0.96^{bA}	0.95 ± 0.02^{bA}	0.95 ± 0.02^{bA}
	97.5	59	95.30 ± 0.96^{bA}	0.95 ± 0.02^{bA}	0.95 ± 0.02^{bA}
	99	59	95.30 ± 0.96^{bA}	0.95 ± 0.02^{bA}	0.95 ± 0.02^{bA}

FDA (frequency-domain approach), RSS (Residual Sum Squares), T^2 (Hotelling T-squared), LA (limit augmentation), CL (control limit), OPCs (optimal number of principal components), A_{cc} (overall accuracy), S_e (sensibility) and S_p (specificity). Results are expressed as mean ± standard error. Different lowercase letters indicate statistically significant differences (95 %) of each goodness of classification metric (A_{cc}, S_e and S_p) as a function of the LA. Uppercase letters indicate statistically significant differences (95 %) of A_{cc}, S_e and S_p as a function of the computed CL.

different CL and LA (Tables 5–7). However, for TFDA-T^2, the residuals of the multifactor ANOVA models performed on S_e and S_p did not meet the assumptions of normality and homoscedasticity, rendering those ANOVA models unsuitable for statistically comparing the PCA-T^2 results at different CL and LA.

In every case (Tables 5–7), the statistical ANOVA procedures were conducted considering the optimized PCA models obtained from the multi-objective optimization process (section 2.8) to simultaneously maximize both S_e and S_p with the lowest number of LVs (Fig. 6). It can be seen in Fig. 6 the typical plateau of the classification metrics via RSS employing TDA (A_{cc}, Fig. 6A, S_e vs S_p, Fig. 6B), FDA (A_{cc}, Fig. 6E, S_e vs S_p, Fig. 6F) and TFDA (A_{cc}, Fig. 6I, S_e vs S_p, Fig. 6J) and for T^2 using TDA (A_{cc}, Fig. 6C, S_e vs S_p, Fig. 6D), FDA (A_{cc}, Fig. 6G, S_e vs S_p, Fig. 6H) and TFDA (A_{cc}, Fig. 6K, S_e vs S_p, Fig. 6L), wherein the multi-objective optimization problem found the OPCs in all cases in the point of crossing of S_e and S_p. The results of TDA (Table 5) showed a great classification performance of control and OC USI. Based on the LSD intervals, the optimized PCA model using RSS with 17 OPCs, employing LA50%-CL90% exhibited high classification performance ($A_{cc} = 95.44$ %, $S_e = 0.96$ and $S_p = 0.95$) with the minimum number of LVs. In contrast, the

Table 7
Optimized Principal Component models (PCA) and statistical performance of the Residual Sum Squares (RSS) and Hotelling's T-squared (T^2) multivariate control statistics for detection of bone fragments using time-frequency domain approach (TFDA).

TFDA-RSS					
LA (%)	CL (%)	OPCs	A_{cc} (%)	S_e	S_p
0	90	6	88.24 ± 1.20^{aA}	0.88 ± 0.03^{aA}	0.89 ± 0.02^{aA}
	95	8	93.02 ± 0.65^{aB}	0.94 ± 0.01^{aB}	0.92 ± 0.02^{aB}
	97.5	9	94.46 ± 0.86^{aC}	0.95 ± 0.02^{aC}	0.94 ± 0.02^{aC}
	99	11	95.42 ± 0.96^{aC}	0.95 ± 0.02^{aC}	0.95 ± 0.02^{aC}
50	**90**	**15**	$\mathbf{96.07 \pm 0.86^{bA}}$	$\mathbf{0.96 \pm 0.01^{bA}}$	$\mathbf{0.96 \pm 0.02^{bA}}$
	95	16	96.03 ± 0.85^{bA}	0.96 ± 0.01^{bA}	0.96 ± 0.02^{bA}
	97.5	19	95.88 ± 0.81^{bA}	0.96 ± 0.01^{bA}	0.96 ± 0.02^{bA}
	99	20	95.81 ± 0.81^{bA}	0.96 ± 0.01^{bA}	0.96 ± 0.02^{bA}
75	90	19	95.81 ± 0.78^{bA}	0.96 ± 0.01^{bA}	0.96 ± 0.02^{bA}
	95	21	95.80 ± 0.87^{bA}	0.96 ± 0.01^{bA}	0.96 ± 0.02^{bA}
	97.5	22	95.77 ± 0.91^{bA}	0.96 ± 0.01^{bA}	0.96 ± 0.02^{bA}
	99	23	95.75 ± 0.84^{bA}	0.96 ± 0.01^{bA}	0.96 ± 0.02^{bA}
100	90	22	95.85 ± 0.80^{bA}	0.96 ± 0.01^{bA}	0.96 ± 0.02^{bA}
	95	24	95.70 ± 0.83^{bA}	0.96 ± 0.01^{bA}	0.96 ± 0.02^{bA}
	97.5	26	95.70 ± 0.86^{bA}	0.96 ± 0.01^{bA}	0.96 ± 0.02^{bA}
	99	28	95.89 ± 0.81^{bA}	0.96 ± 0.01^{bA}	0.96 ± 0.02^{bA}
TFDA-T^2					
LA (%)	CL (%)	OPCs	A_{cc} (%)	S_e*	S_p*
0	90	47	88.20 ± 1.19^{aA}	0.88 ± 0.03	0.88 ± 0.02
	95	50	91.99 ± 0.87^{aB}	0.92 ± 0.02	0.92 ± 0.02
	97.5	51	93.57 ± 1.03^{aC}	0.93 ± 0.02	0.94 ± 0.02
	99	52	94.23 ± 0.85^{aC}	0.94 ± 0.01	0.94 ± 0.02
50	**90**	**59**	$\mathbf{94.58 \pm 1.01^{bA}}$	$\mathbf{0.93 \pm 0.03}$	$\mathbf{0.96 \pm 0.03}$
	95	59	94.54 ± 1.03^{bA}	0.93 ± 0.03	0.96 ± 0.03
	97.5	59	94.54 ± 1.03^{bA}	0.93 ± 0.03	0.96 ± 0.03
	99	59	94.54 ± 1.03^{bA}	0.93 ± 0.03	0.96 ± 0.03
75	90	60	93.09 ± 1.44^{cC}	0.92 ± 0.05	0.94 ± 0.03
	95	60	93.09 ± 1.43^{cC}	0.92 ± 0.05	0.94 ± 0.03
	97.5	60	93.09 ± 1.43^{cC}	0.92 ± 0.05	0.94 ± 0.03
	99	60	93.09 ± 1.43^{cC}	0.92 ± 0.05	0.94 ± 0.03
100	90	61	92.91 ± 2.63^{cC}	0.93 ± 0.08	0.93 ± 0.03
	95	61	92.91 ± 2.63^{cC}	0.93 ± 0.08	0.93 ± 0.03
	97.5	61	92.91 ± 2.63^{cC}	0.93 ± 0.08	0.93 ± 0.03
	99	61	92.91 ± 2.63^{cC}	0.93 ± 0.08	0.93 ± 0.03

TFDA (time-frequency domain approach), RSS (Residual Sum Squares), T^2 (Hotelling T-squared), LA (limit augmentation), CL (control limit), OPCs (optimal number of principal components), A_{cc} (overall accuracy), S_e (sensibility) and S_p (specificity). Results are expressed as mean ± standard error. Different lowercase letters indicate statistically significant differences (95 %) of A_{cc} as a function of the LA. Uppercase letters indicate statistically significant differences (95 %) of A_{cc} as a function of the computed CL. *The residuals from multifactor analysis of variance (ANOVA) models failed to meet the assumptions of normality and homoscedasticity, thus rendering both models unsuitable for practical inference.

Table 8
Classification performance of the Residual Sum Squares (RSS) and Hotelling's T-squared (T^2) multivariate control statistics in the detection of varying-size bone fragments using the time-domain (TDA), frequency-domain (FDA) and time-frequency domain (TFDA) approaches.

TDA		Number of samples (predicted)	
Type	Number of samples (real)	RSS	T^2
2.0 × 1.5 cm	15	15	15
2.0 × 1.0 cm	17	17	17
1.5 × 0.3 cm	**17**	**16**	**16**
1.0 × 0.3 cm	**15**	**14**	**14**
0.5 × 0.3 cm	**17**	**15**	**15**
OC (all types)	81	TP = 78 ± 1 FN = 3 ± 1	TP = 78 ± 1 FN = 3 ± 1
Control (C_{cal+} C_{EV})	81	TN = 77 ± 2 FP = 4 ± 2	TN = 77 ± 2 FP = 4 ± 2
C_{cal}	**73**	TN_{cal} = **71**	TN_{cal} = **71**
C_{EV}	**8**	TN_{IV} = **6**	TN_{IV} = **6**
FDA		Number of samples (predicted)	
Type	Number of samples (real)	RSS	T^2
2.0 × 1.5 cm	15	15	15
2.0 × 1.0 cm	17	17	17
1.5 × 0.3 cm	**17**	17	**16**
1.0 × 0.3 cm	**15**	**14**	**14**
0.5 × 0.3 cm	**17**	**15**	**15**
OC (all types)	81	TP = 78 ± 1 FN = 3 ± 1	TP = 77 ± 1 FN = 4 ± 1
Control (C_{cal+} C_{EV})	81	TN = 78 ± 2 FP = 3 ± 2	TN = 77 ± 2 FP = 4 ± 2
C_{cal}	**73**	TN_{cal} = **72**	TN_{cal} = **71**
C_{EV}	**8**	TN_{IV} = **6**	TN_{IV} = **6**
TFDA		Number of samples (predicted)	
Type	Number of samples (real)	RSS	T^2
2.0 × 1.5 cm	15	15	15
2.0 × 1.0 cm	17	17	17
1.5 × 0.3 cm	**17**	**16**	**15**
1.0 × 0.3 cm	**15**	**14**	**14**
0.5 × 0.3 cm	**17**	**16**	**15**
OC (all types)	81	TP = 78 ± 1 FN = 3 ± 1	TP = 76 ± 2 FN = 5 ± 2
Control (C_{cal+} C_{EV})	81	TN = 78 ± 1 FP = 3 ± 1	TN = 78 ± 2 FP = 3 ± 2
C_{cal}	**73**	TN_{cal} = **72**	TN_{cal} = **72**
C_{EV}	**8**	TN_{IV} = **6**	TN_{IV} = **6**

TDA (time-domain approach), FDA (frequency-domain approach), TFDA (time-frequency domain approach), RSS (Residual Sum Squares), T^2 (Hotelling T-squared), OC (out-of-control), C_{cal} (control images for PCA calibration), C_{EV} (control images for PCA external validation), TP (true positive), TN (true negative), TN_{cal} (true negative for calibration images), TN_{IV} (true negative for external validation images), FP (false positive) and FN (false negative). Results are expressed as mean ± standard error.

optimized PCA model using T^2 required more LVs (OPCs = 55), maintaining the LA50%-CL95 % to achieve similar classification performance to RSS. Closely, the statistical results of FDA (Table 6) exhibited quite similar behavior of TDA, the optimized PCA using RSS with 17 LVs and LA50%-CL95 % showed an A_{cc} = 95.85 %, S_e = 0.96 and S_p = 0.96 and T^2 control statistic reached an A_{cc} = 95.44 %, S_e = 0.95 and S_p = 0.95 using 55 LVs and the same LA and CL of RSS.

As expected, the classification results for TDA and FDA were closely aligned by using both RSS and T^2 (Tables 5 and 6). This result could be attributed to the fact that the presence of BFs produced an important attenuation of the ultrasound energy (Suen et al., 2016). Therefore, the PCA model-based RSS and T^2 were able to satisfactorily detect BF by using both energy-magnitude and energy distribution parameters from the time and frequency domains (as explained in section 3.1). The detection via RSS suggested that the BF presence led to a detectable breakage in the correlation structure of the control model and T^2 indicated extreme values (lower energy related and magnitude values of ultrasound parameters) in these images compared to the control ones (Kruse et al., 2014). Nevertheless, the RSS statistics were the most robust classifier to maximize the goodness of classification of control and OC images due to its simplicity in the use of lower number of LVs than the T^2 statistic (17 vs 55 LVs, respectively; Tables 5–6).

The statistical results of the TFDA approach (Table 7) integrating TDA and FDA ones, slightly improved the classification performance of RSS and did not evidence an important improvement using T^2. In this regard, when model input variables potentially contribute to describing the response, selecting specific input variables can improve model results. Conversely, adding more variables could worsen the model's accuracy (Zhang, 2014). Therefore, the use of TFDA-RSS contributed to not only a slight increase in A_{cc}, S_e and S_p but also to reduced 2 LVs (15 OPCs, Table 7, Fig. 6I and J) maintaining the LA50%-CL95 %. While, in the case of T^2, the combination of TDA and FDA in the same framework to feed the PCA model caused redundance (features which have explained the same extreme values) and promoted the use of more LVs (Fig. 6K and L). This result suggested that the combination of both energy-related and energy-magnitude ultrasound parameters computed in the time and frequency domains made the PCA model more robust for the detection of any disturbance in the correlation structure not only between the variables referred with the energy and distribution in time and frequency domains but also the relationship between both spaces,

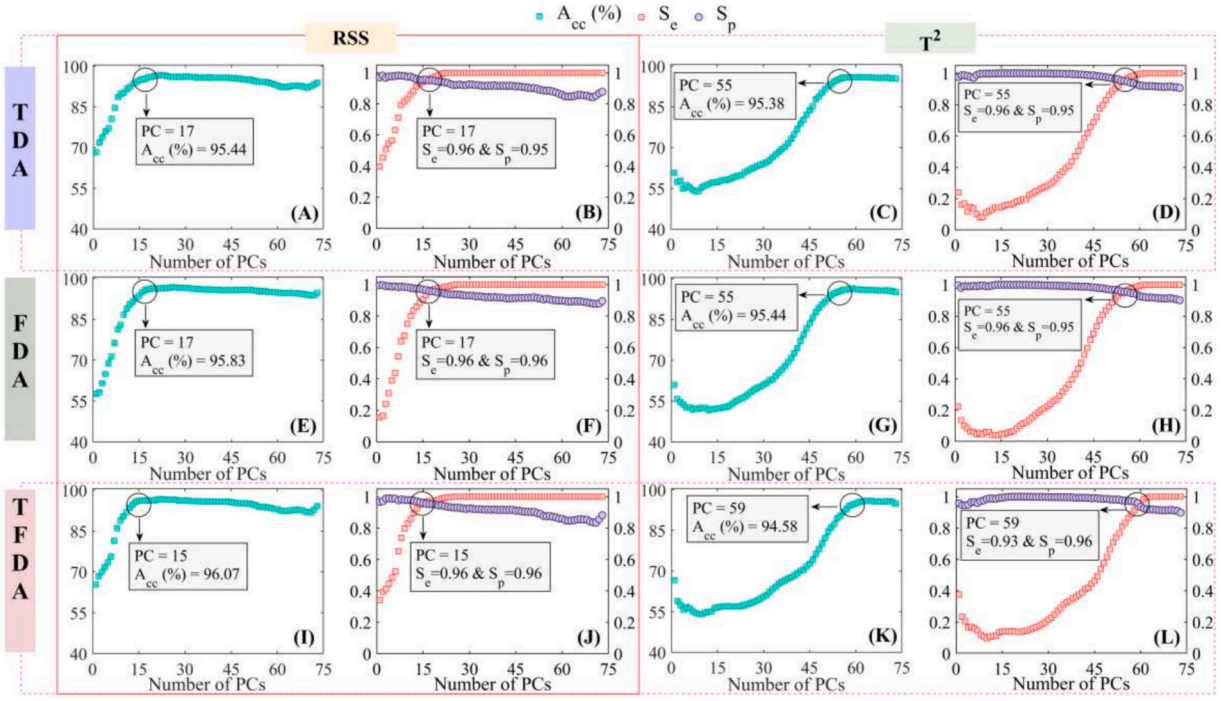

Fig. 6. Classification performance of the multivariate control statistics used for detection of bone fragments in chicken breast fillets. Average A_{cc} for both RSS and T^2 considering TDA (A, C), FDA (E, G) and TFDA (I, K) approaches. Average S_e and S_p for both RSS and T^2 considering TDA (B, D), FDA (F, H) and TFDA (J, L) approaches. TDA (time-domain approach), FDA (frequency-domain approach), TFDA (time-frequency domain approach), A_{cc} (overall accuracy), S_e (sensibility), S_p (specificity), RSS (Residual Sum Squares) and T^2 (Hotelling T-squared).

thus, less LVs were needed to maximize the classification of control and OC images.

To evaluate the classification performance of the LSD based optimized PCA models influenced by the approaches considered, the statistical results in Table 8 illustrate together the CFMs, the number of images correctly classified and misclassified by using both multivariate control statistics. As can be seen, the RSS and T^2 using TDA, FDA and TFDA were able to detect all of OC USI within the larger BFs (2.0 × 1.5 cm and 2.0 × 1.0 cm), while in the detection of the smaller BFs sizes (1.5 × 0.3 cm, 1.0 × 0.3 cm and 0.5 × 0.3 cm), there were 1 ± 1 (from the 100 times randomly partition of data sets) of these OC USI incorrectly classified. Additionally, these optimized models did not correctly classify at least 3 ± 1 control images (from C_{cal} and C_{EV}) in all approaches (Table 8), which can be attributed to the natural variability of poultry meat (Garrido-Novell et al., 2018). The inherent variability such as compositional variations (lean meat and fat components) and intricate structural arrangement (tendons and connective tissues of poultry samples) could contribute to increase variability in control USI (Fariñas, Sanchez-Torres, et al., 2021). Beyond the inherent variability of chicken breast fillets, the occurrence of FN and FP can be further explained by the relationship between the optimization criteria and the model's detection capabilities. In all approaches (TDA, FDA, and TFDA; Fig. 6), the OPCs were selected to achieve a balance by simultaneously maximizing S_e and S_p. This objective meant that the optimal number of LVs did not correspond to the absolute maximum of either S_e or S_p individually. As a result, the model's ability to completely minimize misclassification rates was limited. By applying the methodology proposed in this study and expanding the dataset for model validation, particularly for control samples, more robust and accurate statistical models could be developed (Novack et al., 2024). This would be crucial for addressing the challenges of industrial BF detection in the poultry industry.

As already explained, the use of TFDA-RSS slightly improved the goodness classification metrics compared to TDA-RSS and FDA-RSS. The confidence interval for Acc (96.07 %), based on the dataset used, ranged from 95.74 % to 96.85 %. A narrower confidence interval could be achieved by increasing the sample size. This improvement was achieved by the increase in the detection of one sample within BF of 0.5 × 0.3 cm compared to FDA and the increase in correctly classification of one control image compared to TDA (Table 8). Further, it can also be noticed that FDA-RSS was able to detect all medium-size BFs (1.5 × 0.3 cm). Regarding the T^2 statistic (Table 8), the classification rate of control and OC images did not significantly improve by using TFDA. In addition, the classification performance of RSS and T^2 was equivalent by using TDA and moderate better in RSS compared to T^2 in FDA (reduction of 1 FN and FP by RSS) using lower number of LVs. Thus, either TFDA-RSS or FDA-RSS could be considered as the best option for practical industrial implementation. Results obtained in the present work were similar to those obtained by Zhao et al. (2006) in the detection of glass fragments within beverages packaged in glass containers by the integration of contact ultrasonics and Artificial Neural Networks (ANN). Nonetheless, the differential aspect of this work lies in the capability of the ultrasonic system used in the present work to inspect the entire product, rather than being confined to single-point measurements for detecting foreign bodies. This capability provides a significant advantage in analyzing the presence of foreign bodies, regardless of their location within food products.

Regarding the meat industry, several approaches have been explored for detecting BF in chicken breast fillets. Yoon et al. (2007) used a Near-Infrared (NIR) spectroscopy-based system to identify BF, achieving A_{cc} > 90 %. Similarly, McFarlane et al. (2003) utilized X-ray backscatter techniques to detect clavicles and near-surface BF, reporting detection rates of approximately 85 % < A_{cc} < 95 %. Nevertheless, X-ray-based methods, in general, are characterized by a significant drawback: they are expensive to operate, need costly equipment, pose risks to operators, and require complex post-image processing.

Moreover, spectroscopy-based sensors have also been extensively used to detect food adulteration and contamination. Fengou, Lianou et al. (2021) demonstrated the effectiveness of these sensors in identifying adulteration in minced pork and chicken, with accuracy rates

ranging from 92 % < A_{cc} < 96 %, depending on the type of adulterant and sample preparation. Similarly, Fengou, Tsakanikas et al. (2021) explored the rapid detection of adulterants in minced meat using advanced spectroscopic methods, showcasing their potential for high-throughput applications. These techniques offer rapid, non-destructive detection, but they often require highly specialized equipment and extensive data preprocessing for model calibration and validation. Conversely, the proposed USI combined with MIA offers a cost-effective, safe, and efficient alternative for real-time detection of BF in chicken breast fillets. The classification performance of the USI-MIA approach in this study reached A_{cc} > 95 %, comparable to or exceeding that of X-ray and hyperspectral imaging. Moreover, the non-invasive nature of US, coupled with the minimal post-processing required by MIA, underscores its suitability for industrial-scale implementation.

3.2.1. *Influence of training and validation dataset size on the BF detection*

The statistical results for the detection of BF by using both RSS and T^2 which considered the TDA, FDA and TFDA approaches and four different datasets of total USI (100 %, 75 %, 50 % and 25 %), are depicted in Fig. 7. As can be observed (Fig. 7) the higher the USI in the analysis, the better the performance (progressively increase of A_{cc}, ranging between 80 % to 96 %) of both statistics for all the approaches. The increase in the USI number led to the model becoming more robust with more images for model calibration (Hu et al., 2018). Thus, as can be seen for the RSS, which has provided the best classification results in all of the approaches, the difference between considering the entire batch of samples or 75 % of the total samples, is moderate (< 4 % for TDA and < 3 % for FDA and TFDA, respectively; Fig. 7A, B and C). This fact indicates that the typical plateau value, as observed when plotting A_{cc} versus the number of samples (Hu et al., 2018), has already been reached. The high percentage of correctly classified samples (>95 %) suggests that the number of samples tested in the present study (162, all data) was sufficient to maximize the detection of BFs in the selected approach (TDA, FDA, and/or TFDA) and the RSS multivariate control statistic used.

This study represents an initial step toward developing an accurate and robust quality monitoring system for detecting internal BF in chicken breast fillets. Future research should focus on assessing the detection limit of ultrasound technology in the identification of smallest bone size than the used in this study. To achieve this, it is essential to evaluate the suitability of the frequency employed in the current ultrasound transducer or explore the use of higher frequencies with focused transducers. Additionally, the detection performance of foreign bodies obtained from other materials, such as plastics, metal fragments, and glass, by the integration of USI and MIA is also a significant task that should be assessed. Ultrasonic detection of those foreign bodies could be feasible as long as the acoustic impedance of the object differs from that of the surrounding food. In fact, the use of contact ultrasound has already yielded accurate results for detecting such materials within various food matrices (Hæggström & Luukkala, 2001; Leemans & Destain, 2009; Zhao et al., 2006), thus, the use of USI should be also evaluated.

The integrated use of USI and MIA for detecting BF in poultry meat presents a promising low-cost alternative to traditional technologies based on X-rays and NIR. This approach offers a practical solution for implementation immediately after the chicken deboning line, as the natural surface moisture and physical properties of the chicken fillets facilitate efficient coupling between the transducer and the material. By utilizing array-type transducers, similar to those used in medical ultrasound, the precision and effectiveness of the system can be further enhanced. Adopting this method would not only reduce customer complaints but also ensure consistent product quality and, most importantly, guarantee the safety of the final product.

In the context of food safety, standards set by organizations such as the USDA Food Safety and Inspection Service (FSIS) in the United States and the European Food Safety Authority (EFSA) in the European Union require rigorous monitoring to ensure that processed meat products are free from contaminants and BF. These regulations aim to protect consumers from physical hazards that can lead to injuries or dissatisfaction, while also maintaining trust in food processing systems by minimizing recalls and non-compliance penalties. The development of real-time, non-invasive detection systems, such as the explored in this study, provides the industry with a means to ensure consistent compliance with these quality standards. This research highlights the crucial role of real-time detection systems in actual food processing, demonstrating their advantages over traditional methods in terms of speed, efficiency, non-invasiveness, and seamless adaptability to automation.

4. Conclusions

Contact ultrasound imaging has proven to be an effective and valuable technology for detecting bone fragments of varying sizes, regardless of their location within the chicken breast. The difference in acoustic impedance between the chicken breast and the bone fragments increased energy attenuation, which was linked to the lower ultrasonic velocity and air-filled porous structure of chicken bones. The energy-magnitude and energy-distribution ultrasound parameters, computed in the time-frequency domains, effectively detected the bone fragments within chicken breast fillets. Both temporal and frequency-based approaches quantified similar information regarding ultrasound signal attenuation and alterations in the wave distribution caused by the

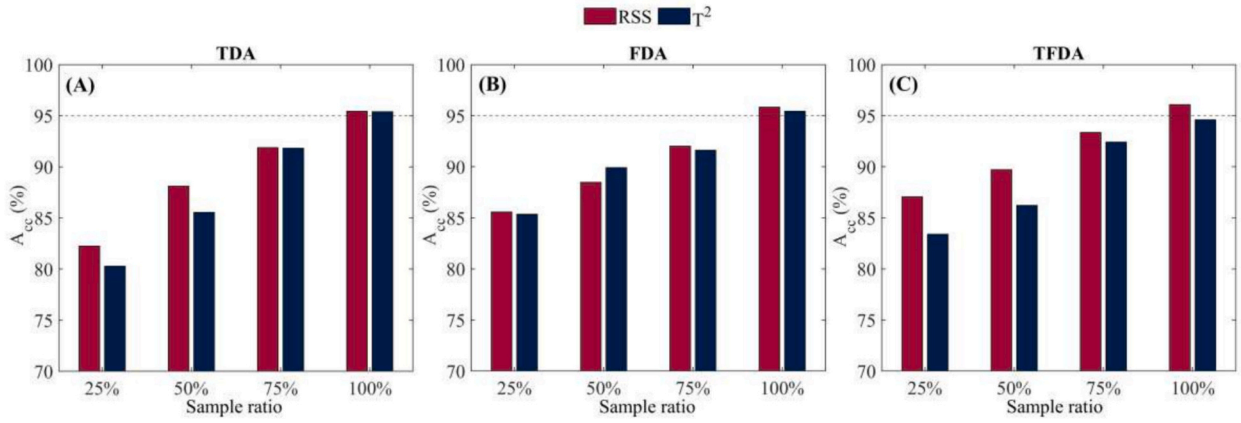

Fig. 7. Average A_{cc} performance of RSS and T^2 control statistics used for detection of bone fragments in chicken breast fillets using different number of ultrasound images. Results for TDA (A), FDA (B) and TFDA (C). TDA (time-domain approach), FDA (frequency-domain approach), TFDA (time-frequency domain approach), A_{cc} (overall accuracy), RSS (Residual Sum Squares) and T^2 (Hotelling T-squared).

presence of varying sizes of bone fragments. The detection of bone fragments was influenced by their size, although good classification results were found for smaller bone fragments.

The Residual Sum Squares multivariate control statistic has proven to be the most robust for detecting bone fragments within chicken breasts, irrespective of the ultrasound parameters (time-frequency) used during the model's tuning. This approach has emerged as a valuable tool for integration into a monitoring system, facilitating the classification of contact ultrasound images of control chicken breasts and those containing bone fragments. Future work should be conducted in order to assess the detection limits of contact ultrasound technology for detecting small-sized bone fragments and to detect foreign bodies of different nature, such as plastics, glass, and metal pieces, which could also contaminate the chicken breast during the manufacturing process. Expanding the dataset would enable the development of more robust and accurate statistical models, which are essential for effective industrial BF detection in the poultry industry. In addition, the development of ultrasonic arrays has to be also addressed in order to improve measurement rate at industrial level. These aspects will be essential to develop a robust industrial prototype that can be used for real-time quality monitoring of the entire poultry meat production.

CRediT authorship contribution statement

Gentil A. Collazos-Escobar: Writing – review & editing, Writing – original draft, Investigation, Formal analysis, Data curation. **Elisa Lincetti:** Writing – original draft, Methodology, Investigation, Data curation, Conceptualization. **Sara Spilimbergo:** Writing – review & editing, Supervision. **José M. Prats-Montalbán:** Writing – review & editing, Methodology, Formal analysis, Data curation. **José V. García-Pérez:** Writing – review & editing, Supervision, Methodology, Formal analysis, Conceptualization. **José Benedito:** Writing – review & editing, Supervision, Methodology, Conceptualization.

Declaration of competing interest

The authors declare that they have no known competing financial interests or personal relationships that could have appeared to influence the work reported in this paper.

Acknowledgments

The authors express their gratitude for the funding provided by the ULTRADIGITAL project (AGROALNEXT/2022/045) as part of the AGROALNEXT program. This program is supported by the MCIN, with funding from the European Union NextGenerationEU (PRTR-C17.I1), as well as the Generalitat Valenciana. Additionally, Gentil A. Collazos-Escobar's doctoral scholarship (PRE2020-092255) is acknowledged, which was granted through the State Training Subprogram of the State Plan for Scientific and Technical Research and Innovation 2017-2020, in conjunction with the European Social Fund.

Data availability

Data will be made available on request.

References

Achata, E. M., Esquerre, C., Gowen, A. A., & O'Donnell, C. P. (2018). Feasibility of near infrared and Raman hyperspectral imaging combined with multivariate analysis to assess binary mixtures of food powders. *Powder Technology, 336*, 555–566. https://doi.org/10.1016/j.powtec.2018.06.025

Aggrey, S. E, Ghareeb, A. F. A, Milfort, M. C, Ariyo, O. W, Aryal, B, Hartono, E, … Rekaya, R (2023). Quantitative and molecular aspects of water intake in meat-type chickens. *Poultry Science, 102*(11). https://doi.org/10.1016/j.psj.2023.102973

Bowler, A., Ozturk, S., di Bari, V., Glover, Z. J., & Watson, N. J. (2023). Machine learning and domain adaptation to monitor yoghurt fermentation using ultrasonic measurements. *Food Control, 147*, Article 109622. https://doi.org/10.1016/j.foodcont.2023.109622

Caesarendra, W., & Tjahjowidodo, T. (2017). *A review of feature extraction methods in vibration-based condition monitoring and its application for degradation trend estimation of low-speed slew bearing.* In machines (Vol. 5, issue 4). MDPI AG. https://doi.org/10.3390/machines5040021.

Caladcad, J. A., Cabahug, S., Catamco, M. R., Villaceran, P. E., Cosgafa, L., Cabizares, K. N., … Piedad, E. J. (2020). Determining Philippine coconut maturity level using machine learning algorithms based on acoustic signal. *Computers and Electronics in Agriculture, 172*. https://doi.org/10.1016/j.compag.2020.105327

Cho, B.-K., & Irudayaraj, J. M. K. (2003). Foreign object and internal disorder detection in food materials using noncontact ultrasound imaging. *Journal of Food Science, 68*.

Colucci, D., Prats-Montalbán, J. M., Fissore, D., & Ferrer, A. (2019). Application of multivariate image analysis for on-line monitoring of a freeze-drying process for pharmaceutical products in vials. *Chemometrics and Intelligent Laboratory Systems, 187*, 19–27. https://doi.org/10.1016/j.chemolab.2019.02.004

Conde, T., Mulet, A., Clemente, G., & Benedito, J. (2008). Detection of internal cracks in manchego cheese using the acoustic impulse-response technique and ultrasounds. *Journal of Dairy Science, 91*(3), 918–927. https://doi.org/10.3168/jds.2007-0661

Corona, E., Garcia-Perez, J. V., Gomez Alvarez-Arenas, T. E., Watson, N., Povey, M. J. W., & Benedito, J. (2013). Advances in the ultrasound characterization of dry-cured meat products. *Journal of Food Engineering, 119*(3), 464–470. https://doi.org/10.1016/j.jfoodeng.2013.06.023

Correia, L. R., Mittal, G. S., & Basir, O. A. (2008). Ultrasonic detection of bone fragment in mechanically deboned chicken breasts. *Innovative Food Science and Emerging Technologies, 9*(1), 109–115. https://doi.org/10.1016/j.ifset.2007.06.004

Craig, A. P., Botelho, B. G., Oliveira, L. S., & Franca, A. S. (2018). Mid infrared spectroscopy and chemometrics as tools for the classification of roasted coffees by cup quality. *Food Chemistry, 245*, 1052–1061. https://doi.org/10.1016/j.foodchem.2017.11.066

Duchesne, C., Liu, J. J., & MacGregor, J. F. (2012). Multivariate image analysis in the process industries: A review. In *, 117. Chemometrics and intelligent laboratory systems* (pp. 116–128). https://doi.org/10.1016/j.chemolab.2012.04.003

Fang, X., Ye, H., Zhang, S., Guo, L., Xu, Y., Zhang, D., & Nie, Q. (2023). Investigation of potential genetic factors for growth traits in yellow-feather broilers using weighted single-step genome-wide association study. *Poultry Science, 102*(11). https://doi.org/10.1016/j.psj.2023.103034

Fariñas, L., Contreras, M., Sanchez-Jimenez, V., Benedito, J., & Garcia-Perez, J. V. (2021). Use of air-coupled ultrasound for the non-invasive characterization of the textural properties of pork burger patties. *Journal of Food Engineering, 297*. https://doi.org/10.1016/j.jfoodeng.2021.110481

Fariñas, L., Sanchez-Torres, E. A., Sanchez-Jimenez, V., Diaz, R., Benedito, J., & Garcia-Perez, J. V. (2021). Assessment of avocado textural changes during ripening by using contactless air-coupled ultrasound. *Journal of Food Engineering, 289*(July 2020). https://doi.org/10.1016/j.jfoodeng.2020.110266

Fariñas, M. D., Sanchez-Jimenez, V., Benedito, J., & Garcia-Perez, J. V. (2023). Monitoring physicochemical modifications in beef steaks during dry salting using contact and non-contact ultrasonic techniques. *Meat Science, 204*, Article 109275. https://doi.org/10.1016/j.meatsci.2023.109275

Fengou, L. C., Lianou, A., Tsakanikas, P., Mohareb, F., & Nychas, G. J. E. (2021). Detection of meat adulteration using spectroscopy-based sensors. *Foods, 10*(4). https://doi.org/10.3390/foods10040861

Fengou, L. C., Tsakanikas, P., & Nychas, G. J. E. (2021). Rapid detection of minced pork and chicken adulteration in fresh, stored and cooked ground meat. *Food Control, 125*. https://doi.org/10.1016/j.foodcont.2021.108002

Gan, W. S. (2020). Signal processing and image processing for acoustical imaging. In *Signal Processing and Image Processing for Acoustical Imaging*. Springer Singapore. https://doi.org/10.1007/978-981-10-5550-8.

Gao, J., Cheng, S., Sun, X., Bai, Y., Yu, X., Zeng, X., Hu, S., Zhang, M., Yue, J., Xu, X., & Han, M. (2024). Combination of contact ultrasound and infrared radiation for improving the quality and flavor of air-dried beef during hot air drying. *Ultrasonics Sonochemistry, 110*. https://doi.org/10.1016/j.ultsonch.2024.107047

Garcia-Perez, J. V., de Prados, M., Martinez, G., Gomez Alvarez-Arenas, T. E., & Benedito, J. (2019). Ultrasonic online monitoring of the ham salting process. Methods for signal analysis: Time of flight calculation. *Journal of Food Engineering, 263*, 87–95. https://doi.org/10.1016/j.jfoodeng.2019.05.032

Garrido-Novell, C., Garrido-Varo, A., Pérez-Marín, D., & Guerrero, J. E. (2018). Using spectral and textural data extracted from hyperspectral near infrared spectroscopy imaging to discriminate between processed pork, poultry and fish proteins. *Chemometrics and Intelligent Laboratory Systems, 172*, 90–99. https://doi.org/10.1016/j.chemolab.2017.11.011

Grassi, S., Jiménez, A., Ruiz, J., & González-Mohino, A. (2024). Use of ultrasound and NIRs as tools for monitoring ice formation in superchilled meat. *Journal of Food Engineering, 369*. https://doi.org/10.1016/j.jfoodeng.2024.111957

Hæggström, E., & Luukkala, M. (2001). Ultrasound detection and identification of foreign bodies in food products. *Food Control, 12*(1), 37–45. https://doi.org/10.1016/S0956-7135(00)00007-4

Hu, M. H., Zhao, Y., & Zhai, G. T. (2018). Active learning algorithm can establish classifier of blueberry damage with very small training dataset using hyperspectral transmittance data. *Chemometrics and Intelligent Laboratory Systems, 172*, 52–57. https://doi.org/10.1016/j.chemolab.2017.11.012

Jiang, H., Yoon, S. C., Zhuang, H., Wang, W., Lawrence, K. C., & Yang, Y. (2018). Tenderness classification of fresh broiler breast fillets using visible and near-infrared hyperspectral imaging. *Meat Science, 139*, 82–90. https://doi.org/10.1016/j.meatsci.2018.01.013

Jiménez-Carvelo, A. M., González-Casado, A., Bagur-González, M. G., & Cuadros-Rodríguez, L. (2019). Alternative data mining/machine learning methods for the analytical evaluation of food quality and authenticity – A review. In *, 122. Food research international* (pp. 25–39). Elsevier Ltd.. https://doi.org/10.1016/j.foodres.2019.03.063

Kruse, O. M. O., Prats-Montalbán, J. M., Indahl, U. G., Kvaal, K., Ferrer, A., & Futsaether, C. M. (2014). Pixel classification methods for identifying and quantifying leaf surface injury from digital images. *Computers and Electronics in Agriculture, 108*, 155–165. https://doi.org/10.1016/j.compag.2014.07.010

Kumar, M., Dahuja, A., Sachdev, A., Kaur, C., Varghese, E., Saha, S., & Sairam, K. V. S. S. (2019). Valorisation of black carrot pomace: microwave assisted extraction of bioactive phytoceuticals and antioxidant activity using Box–Behnken design. Journal of Food Science and Technology, 56(2), 995–1007. Doi: https://doi.org/10.1007/s13197-018-03566-9.

Leemans, V., & Destain, M. F. (2009). Ultrasonic internal defect detection in cheese. *Journal of Food Engineering, 90*(3), 333–340. https://doi.org/10.1016/j.jfoodeng.2008.06.042

Marques, C. D. R., Resende Oliveira, É., Silva Mendes Coutinho, G., Emannuele Chaves Ribeiro, A., Souza Teixeira, C., Soares Soares Júnior, M., & Caliari, M. (2020). Modeling sorption properties of maize by-products obtained using the dynamic Dewpoint isotherm (DDI) method. *Food. Bioscience, 38*(July). https://doi.org/10.1016/j.fbio.2020.100738

McFarlane, N. J. B., Speller, R. D., Bull, C. R., & Tillett, R. D. (2003). Detection of bone fragments in chicken meat using X-ray backscatter. *Biosystems Engineering, 85*(2), 185–199. https://doi.org/10.1016/S1537-5110(03)00036-9

McGrath, T. F., Haughey, S. A., Patterson, J., Fauhl-Hassek, C., Donarski, J., Alewijn, M., … Elliott, C. T. (2018). What are the scientific challenges in moving from targeted to non-targeted methods for food fraud testing and how can they be addressed? – Spectroscopy case study. In *, 76. Trends in food Science and technology* (pp. 38–55). Elsevier Ltd.. https://doi.org/10.1016/j.tifs.2018.04.001

Nielsen, M. S., Lauridsen, T., Christensen, L. B., & Feidenhans'l, R.. (2013). X-ray dark-field imaging for detection of foreign bodies in food. *Food Control, 30*(2), 531–535. https://doi.org/10.1016/j.foodcont.2012.08.007

Novack, A. C., de Cobre, A. F., Stremel, D. P., Ferreira, L. M., Campos, M. L., & Pontarolo, R. (2024). Development and validation of a new method by MIR-FTIR and chemometrics for the early diagnosis of leprosy and evaluation of the treatment effect. *Chemometrics and Intelligent Laboratory Systems, 254*. https://doi.org/10.1016/j.chemolab.2024.105248

Ozturk, S., Bowler, A., Rady, A., & Watson, N. J. (2023). Near-infrared spectroscopy and machine learning for classification of food powders during a continuous process. *Journal of Food Engineering, 341*. https://doi.org/10.1016/j.jfoodeng.2022.111339

Palacio-Niño, J.-O., & Berzal, F. (2019). Evaluation metrics for unsupervised learning algorithms. http://arxiv.org/abs/1905.05667.

Pérez-Santaescolástica, C., Fraeye, I., Barba, F. J., Gómez, B., Tomasevic, I., Romero, A., … Lorenzo, J. M. (2019). Application of non-invasive technologies in dry-cured ham: An overview. In *, 86. Trends in food Science and technology* (pp. 360–374). Elsevier Ltd.. https://doi.org/10.1016/j.tifs.2019.02.011

Prats-Montalbán, J. M., de Juan, A., & Ferrer, A. (2011). Multivariate image analysis: A review with applications. In *, 107, issue 1. Chemometrics and intelligent laboratory systems* (pp. 1–23). https://doi.org/10.1016/j.chemolab.2011.03.002

Reis, M. S. (2015). An integrated multiscale and multivariate image analysis framework for process monitoring of colour random textures: MSMIA. *Chemometrics and Intelligent Laboratory Systems, 142*, 36–48. https://doi.org/10.1016/j.chemolab.2015.01.008

Sanchez-Jimenez, V., Collazos-Escobar, G. A., González-Mohino, A., Alvarez-Arenas, T. E., Benedito, J., & Garcia-Perez, J. V. (2023). Non-invasive monitoring of potato drying by means of air-coupled ultrasound. *Food Control, 109653*. https://doi.org/10.1016/j.foodcont.2023.109653

Sinisterra-Solís, N. K., Sanjuán, N., Ribal, J., Estruch, V., Clemente, G., & Rozakis, S. (2024). Developing a composite indicator to assess agricultural sustainability: Influence of some critical choices. *Ecological Indicators, 161*. https://doi.org/10.1016/j.ecolind.2024.111934

Suen, Y., Xiao, S., Hao, S., Zhao, X., Xiong, Y., & Liu, S. (2016). Time-frequency representation measurement based on temporal Fourier transformation. *Optics Communications, 376*, 86–91. https://doi.org/10.1016/j.optcom.2016.05.017

Sun, H., Zhao, Y., Zhao, J., & Sun, J. (2023). Ultrasound thawing for improving the eating quality and off-flavor of frozen duck meat and its possible mechanisms. *LWT, 187*. https://doi.org/10.1016/j.lwt.2023.115314

Ten-Doménech, I., Pérez-Guaita, D., Quintás, G., & Kuligowski, J. (2023). Analysis of longitudinal data using constrained repeated random sampling-cross validation (CORRS-CV) and partial least squares. *Chemometrics and Intelligent Laboratory Systems, 235*. https://doi.org/10.1016/j.chemolab.2023.104776

Verdú, S., García, I., Roda, C., Barat, J. M., Grau, R., Ferrer, A., & Prats-Montalbán, J. M. (2025). Multivariate image analysis for assessment of textural attributes in transglutaminase-reconstituted meat. *Chemometrics and Intelligent Laboratory Systems, 256*. https://doi.org/10.1016/j.chemolab.2024.105280

Yaqoob, M., Sharma, S., & Aggarwal, P. (2021). Imaging techniques in agro-industry and their applications, a review. In *, Vol. 15, Issue 3. Journal of food measurement and characterization* (pp. 2329–2343). Springer. https://doi.org/10.1007/s11694-021-00809-w.

Yolmeh, M., & Jafari, S. M. (2017). Applications of response surface methodology in the food industry processes. In *, Vol. 10, Issue 3. Food and bioprocess technology* (pp. 413–433). New York LLC: Springer. https://doi.org/10.1007/s11947-016-1855-2.

Zhang, Y. (2014). An improved QSPR method based on support vector machine applying rational sample data selection and genetic algorithm-controlled training parameters optimization. *Chemometrics and Intelligent Laboratory Systems, 134*, 34–46. https://doi.org/10.1016/j.chemolab.2014.03.004

Zhao, B., Yang, P., Basir, O. A., & Mittal, G. S. (2006). Ultrasound based glass fragments detection in glass containers filled with beverages using neural networks and short time Fourier transform. *Food Research International, 39*(6), 686–695. https://doi.org/10.1016/j.foodres.2006.01.008